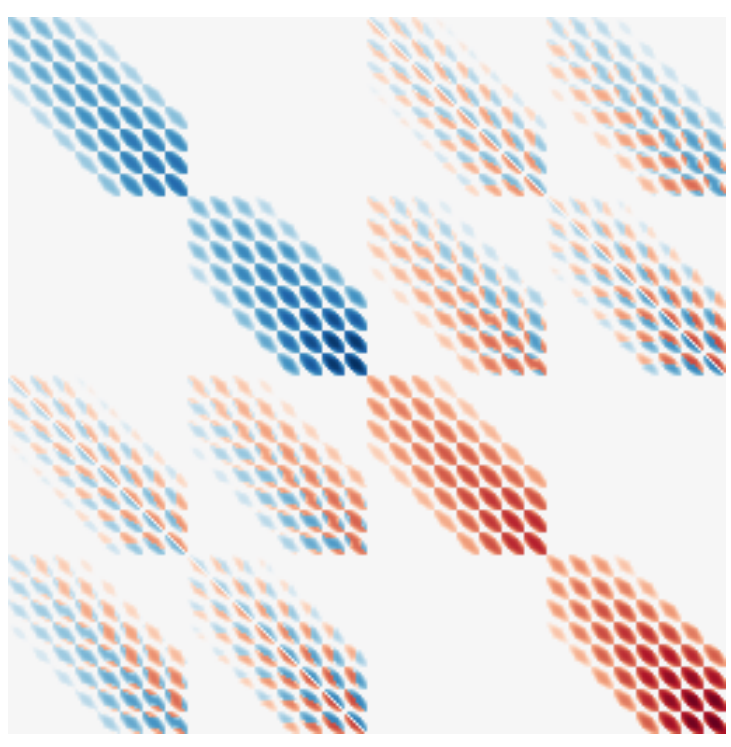


Numerical Resolution of the Dirac Equation **Using B-Spline functions**

Mathis PANET¹

Feb - July 2025

Supervisor: Jean-Philippe Karr² ¹M2 PFA: Quantum Information, ²LKB



Abstract - This internship has been carried out in the "Trapped lons" team at the Laboratoire Kastler Brossel (LKB) under the direction of Jean-Philippe Karr, as part of my Master 2 in Fundamental Physics and Applications (PFA) specialized in Quantum Information at Sorbonne University. The Trapped Ions team is involved in both experimental and theoretical activities, related to high-precision determinations of transition frequencies in simple ions for fundamental physics tests. My work was theoretical and consisted on developing a new method for numerically solving the Dirac Equation. This method relies on the Finite Element Method (FEM) using a specific type of functions called B-Splines. As a first step, it was applied to the hydrogen atom where bound-state energies were obtained with a precision exceeding that of previous numerical studies found in the literature. Then we moved on to the Hydrogen Molecular Ion (HMI), where the implementation of the method is much more complex and is still in progress, although promising preliminary results were obtained. The goal of this work is to prepare the ground for the calculation of the one-loop self-energy QED correction for the HMIs (H₂⁺, HD⁺, ...), which is a crucial step to improve the precision of the value of m_e/m_p from spectroscopy of these ions.

Contents

Abstract								
Acknowledgments								
In	trodu	ection	4					
1	Scientific Context							
	1.1	Fundamental Constants	5					
	1.2	Link between m_e/m_p and HMI energy levels $\dots \dots \dots$	5					
	1.3	Experimental and Theoretical Improvements	6					
	1.4	Relativistic and QED corrections	6					
2	Nun	nerical Resolution of the Dirac Equation	9					
	2.1	The Dirac Equation	9					
	2.2	Expansion in a finite basis	10					
		2.2.1 Dirac Development for the Hydrogen Atom	10					
		2.2.2 Dirac Development for H^2_+	11					
	2.3	FEM method and B-Spline Functions	12					
		2.3.1 Definition and Properties of B-Splines	13					
		2.3.2 Basis Function set for the Hydrogen Atom	14					
		2.3.3 Coordinate System for H_2^+	14					
		2.3.4 Basis Set for H_2^+	15					
	2.4	Numerical Resolution	17					
3	B Results 1							
	3.1	Results for the Hydrogen Atom	18					
	3.2	Results for H_2^+	20					
Co	onclu	sion	22					
Re	eferei	nces	23					
Αŗ	pend	dix	25					
	Α	Matrix Elements of the Dirac Equation for the Hydrogen Atom in DKB	25					
	В	B-Splines: Illustrative Examples	26					
	С	Prolate Spheroidal Coordinates	27					
		C.1 Partial Derivatives	27					
		C.2 Jacobian, Vector Fields and Differential Operators	27					
	D	Example: Integration of element ${f C}_{22}^{(3)}$	29					

Acknowledgments

I would like to express my sincere gratitude to my supervisor, Jean-Philippe Karr, who welcomed me in his group and provided me with the opportunity to work on this project. His guidance, support, and expertise have been invaluable throughout my internship.

I am also grateful for the warm welcome from all the members of the *LKB* group, who made me feel at home and were always willing to help. Especially, I would like to thank the members of the *Trapped lons* team, Laurent Hillico, Maen Salman, Hugo Nogueira and Maxime Leuliet who have answered every and all of my questions, shared their knowledge, and taken the time for coffee breaks.

I would, also, like to thank the professors and staff of the Master of Quantum Information at Sorbonne Université, whose teaching and support have greatly improved my understanding of the field. In particular, I am grateful to Nicolas Treps, the program's director, for his commitment to organizing such a high-quality curriculum and for his help throughout the year. I would especially like to thank him for guiding me toward a great internship that would ultimately shape my career.

Furthermore, many thanks to my classmates with whom I shared countless lectures, study sessions, and discussions. Their support, friendship, and good humor have made this year and all the ones before truly memorable.

Finally, I would like to thank my parents, my brother, family, and friends for their unwavering support and encouragement throughout my academic career. I am profoundly thankful to Marc Panet, my grandfather who instilled in me a passion for research and curiosity, and Nicole Panet, my grandmother who taught me patience and ethics.

A special mention goes to Ryme for her time and patience during the writing of this report.

Introduction

Quantum metrology is the field of study that focuses on the use of quantum phenomena to enhance measurement precision beyond classical limits. Today, a number of fundamental physical constants comes from quantum theory. It is important to improve the determination's the precision of those constants, as they are used in many fields of both fundamental and applied physics. For example, the fine-structure constant α is a dimensionless constant that characterizes the strength of the electromagnetic interaction between elementary charged particles. It comes into play in such diverse phenomena as the quantum Hall effect, the Josephson effect, the fine structure of atomic spectra, atom recoil upon photon absorption, and the electron magnetic moment anomaly. Moreover, it is particularly interesting to measure a given constant by two different methods, as the comparison between the obtained values serves as a test of involved theories and experiments' concistancy, and can be used to search for beyond-standard-model physics.

In recent years, precision spectroscopy of rovibrational transitions in hydrogen molecular ions (HMIs) (H_2^+, HD^+, \ldots) has been used to improve the determination of a fundamental constant, the ratio of the electron mass to the proton mass m_e/m_p [1]. These systems are being studied in quantum metrology experiments in several laboratories, and their theoretical description needs to be refined further. In this context, the goal of this report is to present the work done during my six month internship at Laboratoire Kastler Brossel (LKB) in Paris, France. There, I worked on the development of a new numerical method to resolve the Dirac equation for both the hydrogen atom and the hydrogen molecular ion. The Dirac equation is a relativistic wave equation that describes the behaviour of half-spin particles, such as electrons. In most situations, the Dirac equation doesn't have an analytical solution, and numerical methods are required to solve it. In atomic and molecular physics, the hydrogen atom is the only system where an analytical solution is known, and it is used as a benchmark for testing numerical methods. The resolution of the Dirac equation for the hydrogen molecular ions is the real goal of this work, as it would allow calculating Quantum ElectroDynamics (QED) corrections to their energy levels in a relativistic framework.

The method developed during this internship is based on expanding the wavefunction on a basis of B-splines, which are piecewise polynomial functions that can be used to approximate complex functions. The B-spline basis is well-suited for the resolution of the Dirac equation, as it allows for a high degree of flexibility in the representation of the wave function. Another advantage is that the required matrix elements can be calculated analytically, without the use of numerical integration, thus minimizing numerical errors. Only the diagonalization of the eigenvalue problem is performed numerically.

The report is structured as follows. In the first section, I will present the scientific context of the work, including the current status of the determination of the m_e/m_p fundamental constant and the motivation to study the Dirac equation. In the second section, I will present the theoretical framework of the Dirac equation and the B-spline basis, including the mathematical formulation of the problem and the numerical methods used to solve it. In the third section, I will present the results obtained with the new method, including a comparison with the literature and the previous results of the LKB group. Finally, I will conclude with a discussion of the implications of the results and the next steps for my PhD work, which will be the continuation of this work.

1 Scientific Context

1.1 Fundamental Constants

Recommended values of fundamental constants are established by the *Task Group on Fundamental Physical Constants (TGFC)* of the *Committee on Data of the International Science Council (CODATA)* within the *International Council for Science (ISCU)*. The reference values of the constants, obtained from a least-squares adjustment from the best available experimental data and theoretical calculations, are published every four years.

Atomic and molecular spectra mainly depend on the following constants: the Rydberg constant, the charge radii of the involved nuclei, the electron-to-nucleus mass ratios, and the fine-structure constant. Comparison between precision measurements of transition frequencies and related theoretical predictions can be used to determine some of these constants; for this, it is best to use the simplest species, the spectra of which can be calculated with the highest accuracy. During the last few decades, the precision has improved significantly, due to the development of new experimental techniques and the advancement of theoretical methods. In practice, the Rydberg constant is obtained from spectroscopy of the hydrogen atom, whereas the most precise determination of the proton and deuteron radii was achieved by spectroscopy of muonic hydrogen, where the orbiting electron is replaced by a muon. As for the mass ratios, until recently they were only determined from mass spectrometry measurements performed on single particles or ions in Penning traps. In the last few years, spectroscopy of the hydrogen molecular ion HD $^+$ contributed to improving the precision of the m_e/m_p mass ratio. Its current (CODATA 2022) recommended value is $m_e/m_p = 5.446~170~214~889(94) \times 10^{-4}~[1]$, with a relative uncertainty of 1.7×10^{-11} . This high precision showcases the progress made in the fields of laser spectroscopy and ab initio theory of simple atoms and molecules.

1.2 Link between m_e/m_p and HMI energy levels

The dependence of HMI levels on electron-to-nucleus mass ratios can be understood using a simple model. Within the Bohr-Oppenheimer approximation, one can draw the energy of the ground electronic state of the HMI as a function of the internuclear distance R. This curve will have a minimum corresponding to the equilibrium distance R_e , with a corresponding energy $E_0 \equiv E(R_e)$. Around this minimum, we can expand the energy as a Taylor series. For the argument's sake, we will consider only the second order term, which is the harmonic approximation. In this approximation, the system can be represented by a quantum harmonic oscillator, and the vibrational energy levels of the molecule are given by

$$E_n \approx E_0 + \hbar\omega \left(n + \frac{1}{2} \right) \tag{1.1}$$

where $\omega=\sqrt{k/\mu}$ is the angular frequency of the harmonic oscillator and μ the reduced mass of the nuclei.

For example, in HD⁺, we have $\mu=\mu_{pd}\equiv m_d m_p/(m_d+m_p)$, whereas in H₂⁺, $\mu=m_p/2$. Then, the constant k is proportional to E_h/a_0^2 , where E_h is the Hartree energy, and a_0 the Bohr radius. Using the relationship $1/a_0^2=m_e E_h/\hbar^2$, one gets that the second term in the r.h.s. of eq. (1.1) is proportional to $E_h\sqrt{m_e/\mu}$. This shows that the frequencies of vibrational transitions in H₂⁺ (HD⁺) are approximately proportional to $\sqrt{m_e/m_p}$ ($\sqrt{m_e/\mu_{pd}}$). This is a much stronger dependence than in atomic systems, where the mass ratio only enters in a small isotopic shift, which makes HMIs promising systems to determine these constants.

1.3 Experimental and Theoretical Improvements

In view of HMIs' interest for determination of fundamental constants, the energy levels of these systems have been computed with high precision by solving the three-body *non-relativistic* Schrödinger equation and computing systematically the relativistic and QED corrections (see [2] for example). Additionally, experimental techniques have been developed to measure rovibrational transition frequencies accurately, relying on ion trapping and sympathetic cooling in radiofrequency traps. The figure 1 shows the evolution of the precision for rovibrational transitions of HD⁺ over the years. The recent improvement in experimental precision is due to the development of excitation schemes allowing to perform spectroscopy in the *Lamb-Dicke regime* [3], [4], which allows to eliminate the first-order Doppler broadening.

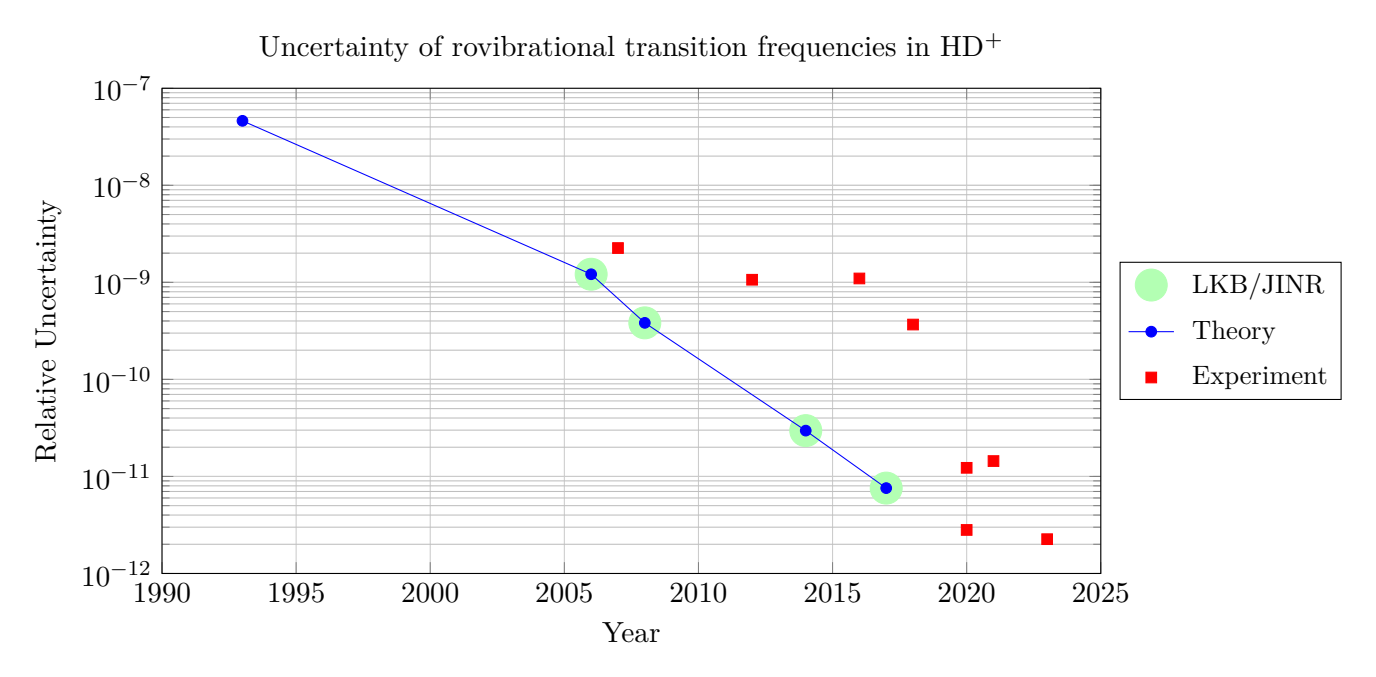


Figure 1: Evolution of the precision of the rovibrational transition frequencies of HD^+ . Currently, the best theoretical precision is achieved by the LKB group in collaboration with Vladimir Korobov (JINR, Dubna, Russia) in 2017 (and updated in 2021) [2]. The last few experimental works have achieved a better precision (eg. [5], [6]).

This advance over the theory highlights the need for more precise theoretical calculations to match the experimental results. The *LKB* group has been working on this problem for several years to reduce the main sources of theoretical uncertainty. One part of this ongoing work involves the numerical resolution of the Dirac equation, which is the focus of this report.

1.4 Relativistic and QED corrections

The theoretical calculations done so far start from the resolution of the three-body Schrödinger equation. Since this equation does not take into account any of the relativistic and QED effects, which are crucial to reach high precision, these corrections are calculated using a systematic perturbative expansion, following an approach called Non Relativistic QED (NRQED). In this approach, the corrections are expanded in terms of three small parameters; α , $Z\alpha$ (where Z is the charge of a nucleus), and m/M (where m and M are respectively the masses of the electron and nucleus). The table 1 gives an example of the contributions one needs to take into account to compute a given transition frequency (here for HD+).

Type of contribution	Framework 3-body	Highest Order	$\Delta \nu_{0,9} ({ m kHz})$ 415 260 910 671.9	
Schrödinger Equation		$m(Z\alpha)^2$		
Relativistic	3-body	$m(Z\alpha)^4$ with recoil	5 667 052.3	
Relativistic	ВО	$m(Z\alpha)^6$	129.6(0.2)	
Relativistic-recoil	3-body	$m(Z\alpha)^5(m/M)$	-320.8	
Relativistic-recoil	3-body	$m(Z\alpha)^6(m/M)$ (partial)	1.2(0.1)	
	3-body	$m\alpha(Z\alpha)^4$ and $m\alpha(Z\alpha)^5$	$-1\ 695\ 245.8$	
One-loop self-energy	ВО	$m\alpha(Z\alpha)^6$	651.1(0.3)	
	ВО	$m\alpha(Z\alpha)^7$ (partial)	-6.3(2.6)	
O 1	3-body	$m\alpha(Z\alpha)^4$ and $m\alpha(Z\alpha)^5$	43 650.3	
One-loop vacuum polarization	ВО	$m\alpha(Z\alpha)^6$ and $m\alpha(Z\alpha)^7$	15.8	
Muonic VP	3-body	Leading Order	1.0	
Hadronic VP	3-body	Leading Order	0.7	
T 1 1::	3-body	$m\alpha^2(Z\alpha)^5$	-272.4	
Two-loop radiative	ВО	$m\alpha^2(Z\alpha)^6$ (partial)	9.4(1.8)	
Three-loop radiative	3-body	$m\alpha^3(Z\alpha)^4$	-0.4	
Radiative recoil	3-body	$m\alpha(Z\alpha)^5(m/M)$	2.1	
Nuclear finite size and	3-body	$m(Z\alpha)^4$	-830.6	
polarizability (+rad. corr.)	3-body	$m(Z\alpha)^6$ (partial)	1.8	
Total value		415 264 925 502.9(3.2) kHz		

Table 1: Contributions to the frequency of the $(\nu, L) = (0, 3) \rightarrow (9, 3)$ transition of HD⁺ [2]. Acronyms: BO = Born-Oppenheimer approximation, VP = vacuum polarization, and rad. corr. = radiative corrections. The total value is given in kHz with an uncertainty in parentheses. The contributions are grouped by type. The orders are given in a system of units where $\hbar = c = 1$.

In this table, following the usual conventions in bound-state QED, we use the system of units where $\hbar=c=m=\epsilon_0=1$, but keep the dependence on m. The order of a contribution is an indication of its magnitude, but also of its type. The power of α is related to the number of QED loops, while the power of $Z\alpha$ is related to the relativistic effects (this comes from the fact that the velocity of the electron is on the order of $v_{el}/c\sim Z\alpha$). Finally, the power of m/M is related to the recoil effects, meaning the effects of nuclear motion (the velocity of a nucleus is on the order of $v_n/c\sim (Z\alpha)(m/M)$).

Corrections that only depend on $Z\alpha$ are purely relativistic corrections, whereas those involving $Z\alpha$ and m/M are called relativistic-recoil corrections. Terms depending on both α and $Z\alpha$ are the radiative corrections. Finally, those involving the three quantities α , $Z\alpha$, and m/M are called radiative-recoil corrections. From table 1, one can see that the largest source of uncertainty is the one-loop self-energy correction of order $m\alpha(Z\alpha)^7$.

The NRQED approach, which takes the Schrödinger equation as a starting point, is used because relativistic QED calculations would be too complicated in a three-body system. However, if one only considers corrections to the bound electron in the Born-Oppenheimer approximation, we have effectively a one-body system (the two nuclei being fixed), and a relativistic QED calculation becomes feasible in principle. In this case, one takes the Dirac (not Schrödinger) equation as a starting point, and does not perform any expansion in powers of $Z\alpha$. In other words, the obtained result will be exact to all orders in $Z\alpha$. In the case of the hydrogen atom, a relativistic calculation of the one-loop self-energy correction yielded a more precise result than the NRQED expansion in powers of $Z\alpha$ [7]. This is why our long-term goal is a relativistic calculation of the one-loop self-energy correction in HMIs, which will hopefully reduce the largest source of uncertainty in table 1. This is our main motivation for numerically solving the Dirac equation.

2 Numerical Resolution of the Dirac Equation

As explained in the introduction, my internship focused on the numerical resolution of the Dirac equation using a Finite Element Method (FEM) and B-Spline functions. The main objective was to develop a numerical method that would allow for the resolution of the Dirac equation for H_2^+ at (a?) very high precision(s?). For future QED corrections' calculations, it is crucial to have a precise numerical representation of the full spectrum of the Dirac equation (energies and wavefunctions).

From now on, we will use the atomic units, which are defined as $\hbar=e=m=4\pi\epsilon_0=1$, but keep the mass m in the expressions.

2.1 The Dirac Equation

The Dirac equation is a fundamental relativistic equation in quantum mechanics that describes the behaviour of half-integer spin particles, such as electrons. The time-independent Dirac equation in an external scalar potential V is given by [8]:

$$\hat{H}\psi\left(\vec{x}\right) = E\psi\left(\vec{x}\right) \quad \text{with } \hat{H} = c\boldsymbol{\alpha} \cdot \boldsymbol{p} + mc^{2}\beta + V\left(\vec{x}\right)\mathbb{I}_{4}$$
 (2.1)

where \hat{H} is the Hamiltonian operator, $\mathbf{p}=-i\boldsymbol{\nabla}$ is the momentum operator, E is the energy, and $\psi\in\mathbb{C}^4$ is the four-spinor wave function. In the chosen unit system, we have $c=1/\alpha$; in all the numerical calculations, we used the CODATA 2022 recommended value [1], $1/\alpha=137.035\,999\,084$.

The matrix structure is given by the Dirac matrices α and β , which are 4×4 matrices given by

$$\alpha_i = \begin{bmatrix} 0 & \sigma_i \\ \sigma_i & 0 \end{bmatrix} \quad \text{and} \quad \beta = \begin{bmatrix} \mathbb{I}_2 & 0 \\ 0 & -\mathbb{I}_2 \end{bmatrix}, \tag{2.2}$$

where σ_i are the usual Pauli matrices.

Writing the four-spinor as $\psi(x) = [\phi(\vec{x}), \chi(\vec{x})]^T$, with $\phi(\vec{x})$ and $\chi(\vec{x})$ respectively the large and small components, the Dirac Equation takes the following form:

$$\underbrace{\begin{bmatrix} V(\vec{x}) + mc^2 & c\boldsymbol{\sigma}.\boldsymbol{p} \\ c\boldsymbol{\sigma}.\boldsymbol{p} & V(\vec{x}) - mc^2 \end{bmatrix}}_{h_D} \underbrace{\begin{bmatrix} \phi(\vec{x}) \\ \chi(\vec{x}) \end{bmatrix}}_{} = E \begin{bmatrix} \phi(\vec{x}) \\ \chi(\vec{x}) \end{bmatrix}$$
(2.3)

To solve the Dirac equation, we will use the Rayleigh-Ritz method [9] in combination with the Finite Element Method (FEM). In this method, the wavefunction is expanded in a finite basis set, and the energy is approximated by the Rayleigh quotient $\langle \psi | \hat{H} | \psi \rangle / \langle \psi | \psi \rangle$. This leads to the following functional equation, which can be obtained by multiplying the Dirac equation by the conjugate transpose of the wave function ψ^{\dagger} on the left and integrating over space:

$$\int \psi^* h_D \psi d^3 x = E \int \psi^* \psi d^3 x \tag{2.4}$$

It is important to note that the application of the Rayleigh-Ritz method in the context of the Dirac equation poses certain problems. Due to the fact that the Dirac spectrum is not bounded from below (it includes both positive and negative-energy continua), it is not assured that the Rayleigh quotient is an upper bound of the exact energy. This can also lead to the appearance of non-physical solutions called *spurious states*. It was found that the convergence of the Rayleigh-Ritz method can be improved by applying so-called *Kinetic Balance* conditions, which consist of imposing specific relationships

between the basis functions used to represent the small and large components [10]. As a first step, we implemented the simplest version of the method where similar basis functions are used for the small and large components without any constraint between them, which we call *No Kinetic Balance* (NKB). In the hydrogen atom case, we also implemented the so-called *Dual Kinetic Balance* (DKB) conditions [11], which have been shown to yield very good convergence and to be well suited for the calculation of QED corrections.

2.2 Expansion in a finite basis

In this section, we write the expansion of the wavefunction ψ in a finite basis set and obtain the matrix form of the Dirac equation for both the hydrogen atom and H_2^+ cases.

2.2.1 Dirac Development for the Hydrogen Atom

Thanks to the spherical symmetry of the hydrogen atom, one can separate the radial (r) and angular coordinates (ρ, ϕ) . More precisely, we can write the wave function as a product of a radial part and an angular part :

$$\psi(\vec{x}) = \frac{1}{r} \begin{bmatrix} \pi^{+}(r)\nu_{\kappa}^{\mu} \\ i\pi^{-}(r)\nu_{-\kappa}^{\mu} \end{bmatrix}$$
 (2.5)

where μ is the quantum number associated with the z-component of the total angular momentum $\mathbf{j}=\mathbf{l}+\mathbf{s}$ (with \mathbf{l} the orbital angular momentum and \mathbf{s} the spin), κ is the Dirac quantum number (see eq. (2.7) below), and ν_{κ}^{μ} are the spherical spinors defined as [12]:

$$\nu_{\kappa}^{\mu}(\hat{\mathbf{r}}) = \begin{pmatrix} -\frac{\kappa}{|\kappa|} \left[\frac{\kappa+1/2-\mu}{2\kappa+1} \right]^{1/2} Y_{|\kappa+1/2|-1/2}^{\mu-1/2}(\hat{\mathbf{r}}) \\ \left[\frac{\kappa+1/2+\mu}{2\kappa+1} \right]^{1/2} Y_{|\kappa+1/2|-1/2}^{\mu+1/2}(\hat{\mathbf{r}}) \end{pmatrix}$$
(2.6)

Here, Y are the spherical harmonics. The value of the quantum number κ is given by:

$$\kappa = \begin{cases}
-\left(j + \frac{1}{2}\right), & j = l + \frac{1}{2} \\
\left(j + \frac{1}{2}\right), & j = l - \frac{1}{2}
\end{cases}$$
(2.7)

We now expand the radial functions $\pi^+(r)$ and $\pi^-(r)$ in a finite basis of size N:

$$\pi^{\pm}(r) = \sum_{i=1}^{N} a_i^{\pm} \pi_i^{\pm}(r)$$
 (2.8)

By injecting (2.8), (2.5) and (2.6) into (2.4), and applying the stationarity condition $\partial E/\partial a_i^\pm=0$, we obtain the following radial equation [13]:

$$\int \begin{bmatrix} \pi_{1}^{+}(r) \\ \vdots \\ \pi_{N}^{+}(r) \\ i\pi_{1}^{-}(r) \\ \vdots \\ i\pi_{N}^{-}(r) \end{bmatrix}^{\dagger} \begin{pmatrix} mc^{2} + V(r) & c\left(\frac{d}{dr} - \frac{\kappa}{r}\right) \\ -c\left(\frac{d}{dr} + \frac{\kappa}{r}\right) & -mc^{2} + V(r) \end{pmatrix} \mathbb{I}_{2N} \begin{bmatrix} \pi_{1}^{+}(r) \\ \vdots \\ \pi_{N}^{+}(r) \\ i\pi_{1}^{-}(r) \\ \vdots \\ i\pi_{N}^{-}(r) \end{bmatrix}^{\dagger} r^{2} dr \begin{bmatrix} a_{1}^{+}(r) \\ \vdots \\ a_{N}^{+}(r) \\ a_{1}^{-}(r) \\ \vdots \\ a_{N}^{-}(r) \end{bmatrix}$$

$$= E \int \begin{bmatrix} \pi_{1}^{+}(r) \\ \vdots \\ \pi_{N}^{+}(r) \\ i\pi_{1}^{-}(r) \\ \vdots \\ i\pi_{N}^{-}(r) \end{bmatrix}^{\dagger} \mathbb{I}_{2N} \begin{bmatrix} \pi_{1}^{+}(r) \\ \vdots \\ \pi_{N}^{+}(r) \\ i\pi_{1}^{-}(r) \\ \vdots \\ i\pi_{N}^{-}(r) \end{bmatrix} r^{2} dr \begin{bmatrix} a_{1}^{+}(r) \\ \vdots \\ a_{N}^{+}(r) \\ a_{1}^{-}(r) \\ \vdots \\ a_{N}^{-}(r) \end{bmatrix}$$
(2.9)

with V(r) the Coulomb potential, which is given by:

$$V(r) = -\frac{Z}{r} \tag{2.10}$$

The integrals in (2.9) correspond to the final form for the *No Kinetic Balance* (NKB) method. The corresponding equation including the DKB conditions is given in Appendix A.

2.2.2 Dirac Development for H₊²

In the case of the hydrogen molecular ion, we can use the cylindrical coordinates (ρ, θ, z) . Thanks to the cylindrical symmetry of the problem, the components of the wave function can be written as a product of a radial part and an angular part. More precisely, we can write $\psi(\vec{x})$ as:

$$\psi(\vec{x}) = \begin{bmatrix} \phi^{(1)}(\rho, z) e^{i(j_z - \frac{1}{2})\theta} \\ \phi^{(2)}(\rho, z) e^{i(j_z + \frac{1}{2})\theta} \\ i\chi^{(1)}(\rho, z) e^{i(j_z - \frac{1}{2})\theta} \\ i\chi^{(2)}(\rho, z) e^{i(j_z + \frac{1}{2})\theta} \end{bmatrix}$$
(2.11)

where j_z is the quantum number associated with the z-component of the total angular momentum $\mathbf{j} = \mathbf{l} + \mathbf{s}$. Here, j_z is a half-integer number, which is a consequence of the half-spin of the electron.

One can develop $\sigma.p$ in cylindrical coordinates from the definition of the Pauli matrices:

$$c\boldsymbol{\sigma}.\boldsymbol{p} = -ic\boldsymbol{\sigma}.\boldsymbol{\nabla} \tag{2.12}$$

$$= -ic \begin{pmatrix} \partial_z & \partial_x - i\partial_y \\ \partial_x + i\partial_y & -\partial_z \end{pmatrix}$$
 (2.13)

$$= -ic \begin{pmatrix} \partial_z & \partial_x - i\partial_y \\ \partial_x + i\partial_y & -\partial_z \end{pmatrix}$$

$$= -ic \begin{pmatrix} \partial_z & e^{-i\theta} \left(\partial_\rho - i\frac{\partial_\theta}{\rho} \right) \\ e^{i\theta} \left(\partial_\rho + i\frac{\partial_\theta}{\rho} \right) & -\partial_z \end{pmatrix}$$
(2.13)

Similarly to the previous section, we expand the four components of the radial wave function as:

$$\begin{cases} \phi^{(1,2)} &= \sum_{n=1}^{N} a_n^{(1,2)} \phi_n^{(1,2)} \\ \chi^{(1,2)} &= \sum_{n=1}^{N} c_n^{(1,2)} \chi_n^{(1,2)} \end{cases}$$
(2.15)

Injecting (2.11), (2.14), and (2.15) into (2.4), and applying the stationarity condition $\partial E/\partial a_n^{(1,2)}=\partial E/\partial c_n^{(1,2)}=0$, one gets:

$$\mathbf{C}\mathbf{v} = E\mathbf{S}\mathbf{v},\tag{2.16}$$

where ${\bf v}$ is a vector composed of the coefficients to be determined; ${\bf C}$ and ${\bf S}$ are $4N\times 4N$ matrices , which have the following structure:

$$\mathbf{C} = \begin{pmatrix} \mathbf{C}^{(1)} & \mathbf{C}^{(3)} \\ \mathbf{C}^{(3)\mathrm{T}} & \mathbf{C}^{(2)} \end{pmatrix} = \begin{pmatrix} \mathbf{C}_{11}^{(1)} & \mathbf{C}_{12}^{(1)} & \mathbf{C}_{11}^{(3)} & \mathbf{C}_{12}^{(3)} \\ \mathbf{C}_{21}^{(1)} & \mathbf{C}_{22}^{(1)} & \mathbf{C}_{21}^{(3)} & \mathbf{C}_{22}^{(3)} \\ \mathbf{C}_{11}^{(3)\mathrm{T}} & \mathbf{C}_{21}^{(3)\mathrm{T}} & \mathbf{C}_{12}^{(2)} & \mathbf{C}_{12}^{(2)} \\ \mathbf{C}_{12}^{(3)\mathrm{T}} & \mathbf{C}_{22}^{(3)\mathrm{T}} & \mathbf{C}_{21}^{(2)} & \mathbf{C}_{22}^{(2)} \end{pmatrix},$$
(2.17)

$$\mathbf{S} = \begin{pmatrix} \mathbf{S}^{(1)} & 0 \\ 0 & \mathbf{S}^{(2)} \end{pmatrix} = \begin{pmatrix} \mathbf{S}_{11}^{(1)} & 0 & 0 & 0 \\ 0 & \mathbf{S}_{22}^{(1)} & 0 & 0 \\ 0 & 0 & \mathbf{S}_{11}^{(2)} & 0 \\ 0 & 0 & 0 & \mathbf{S}_{22}^{(2)} \end{pmatrix}$$
(2.18)

Each element of the above 4×4 matrices is itself a $N \times N$ matrix. The elements of all these $N \times N$ sub-matrices are given by:

$$[\mathbf{C}^{(1)}]_{i,j} = \int \begin{pmatrix} \phi_i^{(1),*} \left(V + mc^2 \right) \phi_j^{(1)} & 0 \\ 0 & \phi_i^{(2),*} \left(V + mc^2 \right) \phi_j^{(2)} \end{pmatrix} \rho d\rho dz, \tag{2.19}$$

$$[\mathbf{C}^{(2)}]_{i,j} = \int \begin{pmatrix} \chi_i^{(1),*} \left(V - mc^2 \right) \chi_j^{(1)} & 0 \\ 0 & \chi_i^{(2),*} \left(V - mc^2 \right) \chi_j^{(2)} \end{pmatrix} \rho d\rho dz, \tag{2.20}$$

$$[\mathbf{C}^{(3)}]_{i,j} = c \int \begin{pmatrix} \phi_i^{(1),*} \partial_z \chi_j^{(1)} & \phi_i^{(1),*} \left(\partial_r + \frac{(j_z + \frac{1}{2})}{r} \right) \chi_j^{(2)} \\ \phi_i^{(2),*} \left(\partial_r - \frac{(j_z - \frac{1}{2})}{r} \right) \chi_j^{(1)} & -\phi_i^{(2),*} \partial_z \chi_j^{(2)} \end{pmatrix} \rho d\rho dz, \tag{2.21}$$

$$[\mathbf{S}^{(1)}]_{i,j} = \int \begin{pmatrix} \phi_i^{(1),*} \phi_j^{(1)} & 0\\ 0 & \phi_i^{(2),*} \phi_j^{(2)} \end{pmatrix} \rho d\rho dz, \tag{2.22}$$

$$[\mathbf{S}^{(2)}]_{i,j} = \int \begin{pmatrix} \chi_i^{(1),*} \chi_j^{(1)} & 0\\ 0 & \chi_i^{(2),*} \chi_j^{(2)} \end{pmatrix} \rho d\rho dz$$
(2.23)

where $V = -Z_1/r_1 - Z_2/r_2$. The integrals are computed over the whole space, but in practice, we will use a finite domain to compute the integrals numerically.

The few zero elements of the matrices C and S are due to the angular part of the wave function, which is orthogonal for different values of j_z (cf. 2.11).

2.3 FEM method and B-Spline Functions

The Finite Element Method (FEM) is a numerical technique used to find approximate solutions to partial differential equations by discretizing the domain into smaller, simpler parts called finite elements. The main idea is to approximate the solution by a linear combination of basis functions defined on these elements.

We, thus, rewrite (2.15) as

$$\begin{cases} \phi^{(1,2)} &= \sum_{n=1}^{N} a_n^{(1,2)} B_n^{(1,2)} \\ \chi^{(1,2)} &= \sum_{n=1}^{N} c_n^{(1,2)} B_n^{(1,2)} \end{cases}$$
(2.24)

where N is the number of basis functions used to approximate the wave function, $B_n^{(1,2)}(\vec{x})$ are the B-spline basis functions, and $a_n^{(1,2)}$ and $c_n^{(1,2)}$ are the coefficients to be determined. The chosen basis functions will be detailed below.

2.3.1 Definition and Properties of B-Splines

B-spline functions are a family of piecewise polynomial functions that are widely used in numerical analysis and computer graphics. They are defined by a set of knots and a degree, which determines the polynomial order of the piecewise segments.

To construct a B-spline basis of degree k with a set of knots $\{x_0, x_1, \dots, x_{N-1}\}$, we can use the Cox-de Boor recursion formula [14]:

$$b_{i,k}^{\{x_j\}}(x) = \frac{x - x_i}{x_{i+k} - x_i} b_{i,k-1}^{\{x_j\}}(x) + \frac{x_{i+k+1} - x}{x_{i+k+1} - x_{i+1}} b_{i+1,k-1}^{\{x_j\}}(x)$$
(2.25)

with the initial B-spline functions defined as:

$$b_{i,1}^{\{x_j\}}(x) = \begin{cases} 1 & \text{if } x_i \le x < x_{i+1} \\ 0 & \text{otherwise} \end{cases}$$

To produce a complete basis set, we need to define a set of knots $\{x_0, x_1, \dots, x_{N-1}\}$, where N is the number of knots and a fixed degree k for the B-spline functions. Once it is done, a complete basis set of B-spline functions will be made of N-k-2 B-spline functions. Thus, in equation (2.25), the index i will run from 0 to N-k-3.

Examples of B-spline functions and bases for different orders are presented in Appendix B.

B-splines are particularly useful for approximating functions and solving differential equations in atomic and molecular physics computations due to their desirable properties [15], such as:

- Compact support: Each $b_{i,k}(x)$ is non-zero only on the interval $[x_i, x_{i+k+1}]$, resulting in sparse matrices upon discretization of differential operators.
- Continuity control: A spline of degree k is globally C^{k-2} continuous across knot locations, ensuring sufficient smoothness for accurate representation of wavefunctions.
- Partition of unity: The set of basis functions satisfies $\sum_i b_{i,k}(x) = 1$ for all x, preserving normalization and preventing the introduction of spurious behaviour. This is a different type of normalization than the ones we typically use in physics but it has the same consequence: preventing the numerical values from exploding.
- Flexible knot placement and multiplicity: The knot vector may be non-uniform, allowing finer resolution in specific regions of the domain, such as near the nuclei. Furthermore, repeated knots can be used to maximise flexibility locally, which is useful for representing features like singularities or discontinuities in the wavefunction or potential.

In practice, B-spline expansions have demonstrated exceptional performance in solving the Schrödinger equation for both bound and continuum states within a unified framework [15]. Consequently, B-spline basis sets have become a standard tool in high-precision atomic and molecular calculations.

In our case, we will use B-spline functions because of the properties mentioned above, which are particularly useful for the resolution of the Dirac equation. They allow high precision calculations of both bound and continuum states, which is a prerequisite for the calculation of the one-loop self-energy correction.

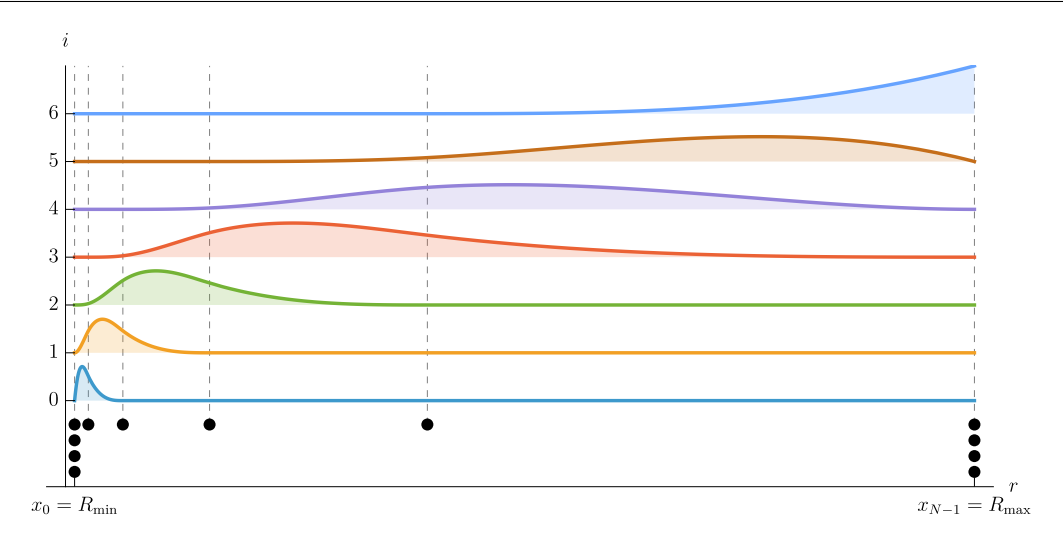


Figure 2: Distribution of the knots for the radial coordinate r of the hydrogen atom with k = 4 and N = 12. The coloured curve represent the different basis function.

2.3.2 Basis Function set for the Hydrogen Atom

In this system, we only need to consider one coordinate, the radial coordinate r. This allows us to choose a simple set of basis functions, which are the B-spline functions:

$$B_n^{(1)}(r) = B_n^{(2)}(r) = b_{n,k}^{\{x_j\}}(r)$$
(2.26)

The B-spline basis functions are defined on the interval $[R_{\min}, R_{\max}]$, where R_{\min} is the position of the closest knot to the nucleus and R_{\max} is the maximum radius we want to consider. Since the characteristic size of the electron wavefunction is the Bohr radius a_0 , we need to take $R_{\max} \gg a_0$. To maximize the precision of the numerical resolution for bound states, the most interesting region is $0 \le r \le a_0$. On the other hand, due to the singularity of the Coulomb potential at the position of the nucleus, we can't place a knot at the position of the nucleus, as it would lead to numerical issues when evaluating the potential matrix element around the nucleus. Thus, we have chosen to distribute the knots using a geometric progression, which allows us to have more knots in the region of interest while extending the description of the wave function to a larger region. However, to better cover the entire interval, we need to place k knots on each border. Thus, the knots are defined as:

$$x_{i} = \begin{cases} R_{\min} \cdot \left(\frac{R_{\max}}{R_{\min}}\right)^{\frac{i}{N-1}}, & i = k, \dots, N - k - 1\\ R_{\min}, & i = 0, \dots, k - 1\\ R_{\max}, & i = N - k, \dots, N - 1 \end{cases}$$
(2.27)

where N is the number of knots, k the order of the B-Spline basis, and R_{\min} should be different from zero. An example of the distribution of the knots is presented in Figure 2.

2.3.3 Coordinate System for H₂⁺

So far, for H_2^+ , we have used the cylindrical coordinate system (r, θ, z) . As seen before, the symmetry of the problem allows us to separate out the angular variable θ . From now on, we will instead use the prolate spheroidal coordinates

 (ξ, η, θ) , which are defined as [16]:

$$\begin{cases} \xi = \frac{1}{2R} \left(\sqrt{x^2 + y^2 + (z+R)^2} + \sqrt{x^2 + y^2 + (z-R)^2} \right) \\ \eta = \frac{1}{2R} \left(\sqrt{x^2 + y^2 + (z+R)^2} - \sqrt{x^2 + y^2 + (z-R)^2} \right) \end{cases}$$
(2.28)

where R is the distance between the two nuclei, $\xi \in [1,\infty)$ is the radial coordinate, $\eta \in [-1,1]$ is the axial coordinate. The last coordinate $\theta \in [0,2\pi[$ is the same as in the cylindrical coordinate system (azimuthal angle). A representation of the radial coordinate system via contour lines is shown in Figure 3. More relationships between the prolate spheroidal coordinates and other coordinate systems, including expressions of differential operators, can be found in Appendix C.

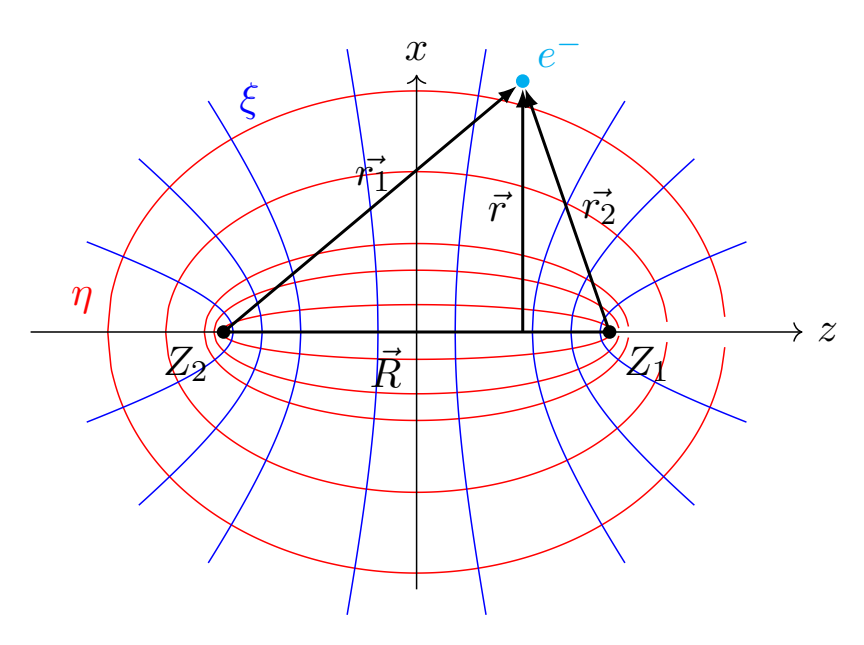


Figure 3: Prolate Spheroidal Coordinate System for the case of Hydrogen Molecular Ions.

The prolate spheroidal coordinates are particularly useful in the context of H_2^+ . Just like the cylindrical coordinates, they allow us to separate out the θ coordinate. Moreover, they are well suited to the two-center problem, as they put the nuclei at the extremities of the η axis. This is extremely useful because the Coulomb potential is singular at their positions, and thus, it is better to have them at the extremities of the coordinate system. This allows us to avoid numerical issues when evaluating the potential matrix elements around the nuclei.

Using this coordinate system, we can write the two-nuclei Coulomb potential as:

$$V(\xi, \eta) = -\frac{Z_1}{R(\xi - \eta)} - \frac{Z_2}{R(\xi + \eta)}$$
(2.29)

2.3.4 Basis Set for H_2^+

We need to define a set of basis functions that can describe the wave function for the two remaining coordinates (ξ, η) . The general idea is to use products of B-spline functions of each coordinate. However, in order to better represent the short-range behaviour of the wave function, which depends on the quantum number j_z , we add a j_z -dependent factor

to the B-spline functions [17]. This leads to the following definition of the basis functions:

$$\begin{cases}
B_{i,i'}^{(1)}(\xi,\eta) &= \left((\xi^2 - 1)(1 - \eta^2) \right)^{\frac{jz+1/2}{2}} \cdot b_{i,k}^{\{x_j\}}(\xi) \cdot b_{i',k}^{\{y_j\}}(\eta) \\
B_{i,i'}^{(2)}(\xi,\eta) &= \left((\xi^2 - 1)(1 - \eta^2) \right)^{\frac{jz-1/2}{2}} \cdot b_{i,k}^{\{x_j\}}(\xi) \cdot b_{i',k}^{\{y_j\}}(\eta)
\end{cases}$$
(2.30)

Now, we need to choose carefully the interval for the two coordinates ξ and η . ξ is a similar situation to the radial coordinate r for the hydrogen atom, so we can use an interval $[\xi_{\min}, \xi_{\max}]$, with $\xi_{\max} \gg 1$. However, in this case, ξ_{\min} should tend to one instead of zero, as the minimum value of ξ is one. The maximum value of ξ is not fixed, but we can take a large enough value to cover the region of interest. For η , the situation is different, as it is related to an angle and can take values between -1 and 1. Thus, we need to cover the whole interval]-1,1[(without the two extremities).

For the knot distribution, we can use the same geometric progression as (2.27) for ξ , but we need to adapt it for η . After several tests, we found that a symmetric distribution around 0 with a geometric progression works well. It allows us to maximize the number of knots around the two nuclei and, for more control, the geometric sequence is adjusted by a parameter a that controls the distribution of the knots. Thus, we can define the knots for ξ and η as:

$$x_{i} = \begin{cases} \xi_{\min} \cdot \left(\frac{\xi_{\max}}{\xi_{\min}}\right)^{\frac{i}{N-1}}, & i = k, \dots, N - k - 1\\ \xi_{\min}, & i = 0, \dots, k - 1\\ \xi_{\max}, & i = N - k, \dots, N - 1 \end{cases}$$
(2.31)

$$x_{i} = \begin{cases} \xi_{\min} \cdot \left(\frac{\xi_{\max}}{\xi_{\min}}\right)^{\frac{i}{N-1}}, & i = k, \dots, N - k - 1 \\ \xi_{\min}, & i = 0, \dots, k - 1 \\ \xi_{\max}, & i = N - k, \dots, N - 1 \end{cases}$$

$$y_{i} = \begin{cases} a - 1, & 0 \le i < k \\ a\left(\frac{1}{a}\right)^{\frac{2i}{N}} - 1, & k \le i < \frac{N}{2} \\ 1 - a\left(\frac{1}{a}\right)^{\frac{2i}{N}}, & \frac{N}{2} \le i < N - k \\ 1 - a, & N - k \le i < N \end{cases}$$

$$(2.31)$$

An example of the knot distribution is shown in Figure 4. The parameter a controls the distribution of the knots around the two nuclei, and it corresponds to the position of the closest knots to ± 1 for η .

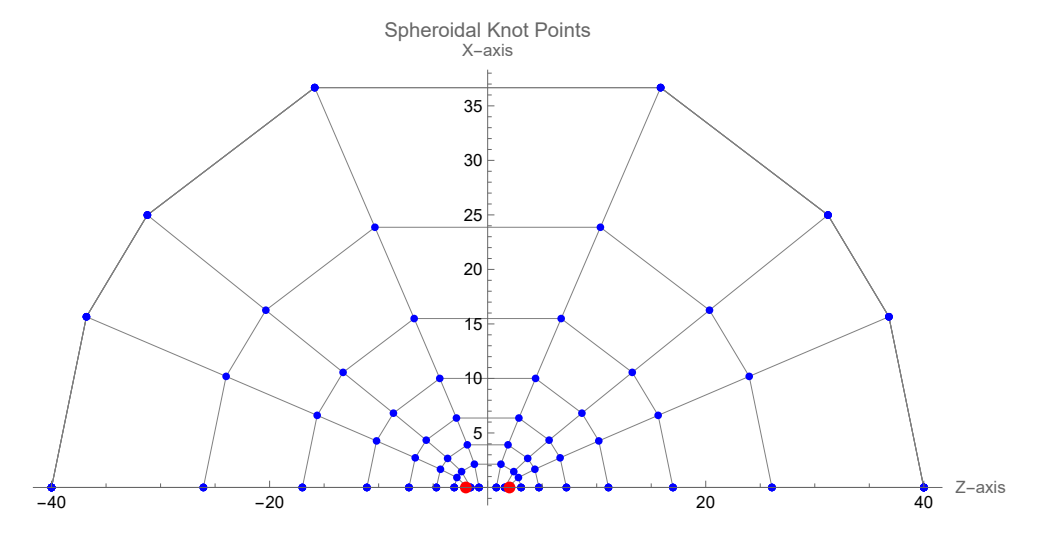


Figure 4: Distribution of the knots using the prolate spheroidal coordinate system (ξ, η) for H_2^+ . The knots are distributed using a logarithmic scale for ξ and a symmetric distribution around 0 for η with parameter $a = 4 \times 10^{-2}$. The number of knots is N = 10 for both coordinates.

2.4 Numerical Resolution

To achieve very high precision in the numerical resolution of the Dirac equation, we want to avoid any loss of precision in the evaluation of matrix elements. This is why we don't use any method of numerical integration, such as the trapezoidal rule or a quadrature method, to compute the integrals. Instead, we use an automatic algebraic integration method, which allows us to compute the integrals exactly. More precisely, we do the integration piece by piece, which means that we can consider each involved B-spline function as a polynomial on a small portion of the space. Then, each term of the polynomial is integrated independently, using a general formula produced by $\mathtt{Mathematica}$ [18]. An example for one element of the matrix $\mathbf{C}^{(1)}$ for \mathbf{H}_2^+ is given in Appendix D.

This method allows us to compute the integrals with very high precision, as it avoids any numerical approximation. The only limitation is the precision of the floating-point representation. This is why we are implementing the code in Fortran with the arbitrary precision arithmetic library MPFUN2020 [19].

This package is particularly useful but it increases the computation time by a large factor. To overcome this issue, the code was developed to be parallelized. The parallelization is done using the OpenMP library, which allows us to use multiple threads to compute the integrals in parallel. Our problem is particularly well adapted to parallelization, as each element of the matrix C (resp. S) can be computed independently.

Once the matrices C and S are computed, we find ourselves with a generalized eigenvalue problem of the form:

$$\mathbf{C}\mathbf{v} = E\mathbf{S}\mathbf{v} \tag{2.33}$$

where ${\bf v}$ is the eigenvector corresponding to the eigenvalue E.

This problem can be solved using the LAPACK library [20], which is a library for solving large-scale eigenvalue problems. However, the LAPACK library is not compatible with the MPFUN2020 library. The LKB team was previously using a diagonalization subroutine developed by V. Korobov from the rsg subroutine of the EISPACK package. Recently, Hugo Nogueira developed a parallelized version of this subroutine that is compatible with the MPFUN2020 library. This allows us to solve the generalized eigenvalue problem with arbitrary precision arithmetic.

3 Results

In this section, we present the results obtained from the numerical resolution of the Dirac equation using B-spline functions. The focus is, for now, on the values of the eigenvalues representing the energy levels of the system.

For an electron in a binding potential, the eigenvalues can be classified into three groups: a positive-energy continuum above the rest mass energy (mc^2) , a negative-energy continuum below $(-mc^2)$, and discrete eigenvalues between $(-mc^2)$ and (mc^2) . We are particularly interested in the last group, which corresponds to the bound states and can be used to study the convergence and to be compared with literature values to validate our numerical results. The eigenvalues in the other groups correspond to the free states of the system; our calculations provide a numerical representation of the continuum. The negative eigenvalues are often referred to as the Dirac Sea, which is a theoretical model of antiparticles in quantum field theory [21].

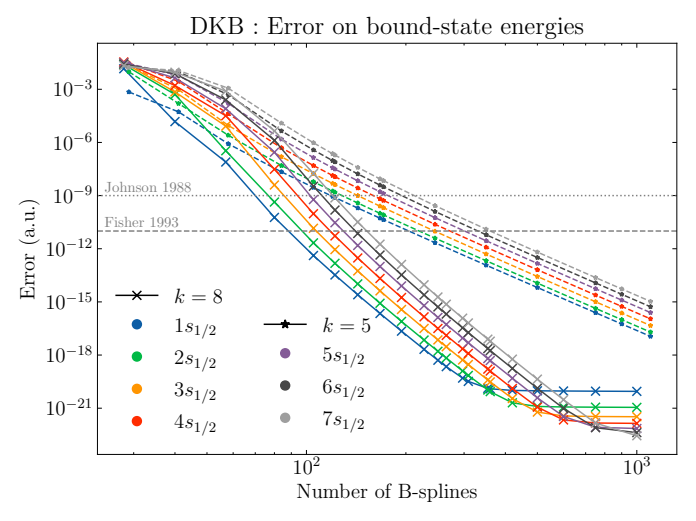
3.1 Results for the Hydrogen Atom

As stated before, the Dirac equation for the hydrogen atom can be solved analytically [22]. The bound-state energies are given by:

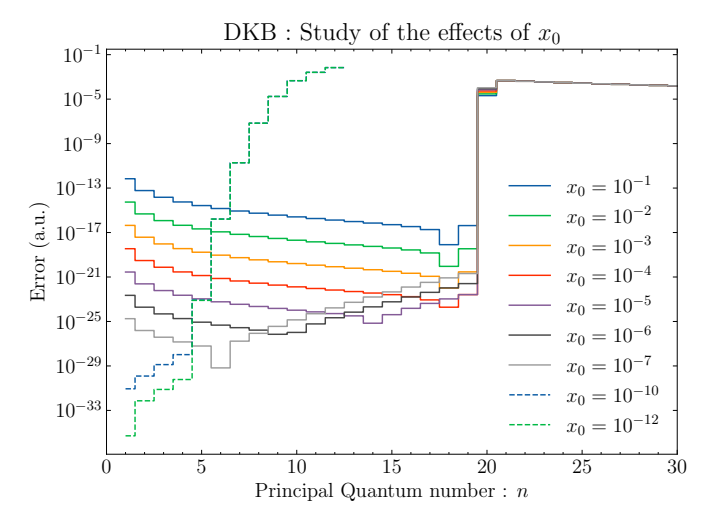
$$E_n = \frac{mc^2}{\sqrt{1 + \left(\frac{Z/c}{n - |\kappa| + \sqrt{\kappa^2 - \left(\frac{Z}{c}\right)^2}}\right)^2}}$$
(3.1)

where n is the principal quantum number.

Thanks to this, we can perfectly evaluate the accuracy of our numerical method by comparing the obtained results with the analytical solution. There are several parameters that can be adjusted in the numerical method but we will restrict ourselves to showing the impact of the knot distribution explained in section 2.3.2. The main parameters that we will vary



(a) Error on the lowest $ns_{1/2}$ bound-state energies obtained with the DKB method for different orders of B-spline functions. The two grey horizontal lines represent the best precisions from numerical calculations reported in the literature ([23], [24]). For $x_0 = 10^{-6}$ a.u. and $x_{max} = 200$ a.u.



(b) Error on the lowest $ns_{1/2}$ bound-state energies obtained for different values of n and x_0 . For k=8, $x_{max}=500$ a.u. and N=800.

Figure 5: Results for the DKB method.

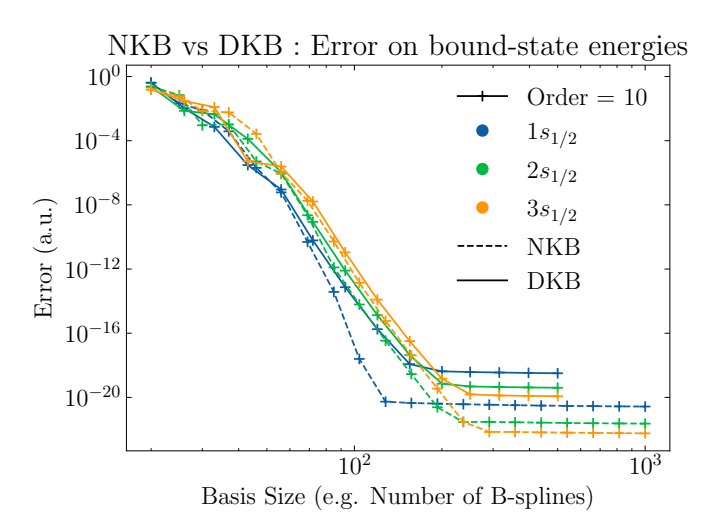
are the number of knots, the position of the first and last knots, and the order of the B-spline functions. Furthermore, we will compare the results obtained with the *No Kinetic Balance* (NKB) method and the *Dirac Kinetic Balance* (DKB) method.

The figure 5a shows the error on the energies of the first few $s_{1/2}$ ($\kappa=-1$) bound states obtained with the DKB method for different orders of B-spline functions using a very large integration domain ($R_{max}=200$ a.u.). The error is defined as the absolute value of the difference between the numerical eigenvalue and the analytical one. For both k=5 and k=8 orders, our results far exceed the best precisions reported from numerical calculations in the literature ([23], [24]). The order k=8 converges significantly faster than k=5, but requires a longer computation time (for the same basis size) as the calculation of matrix elements is more complex.

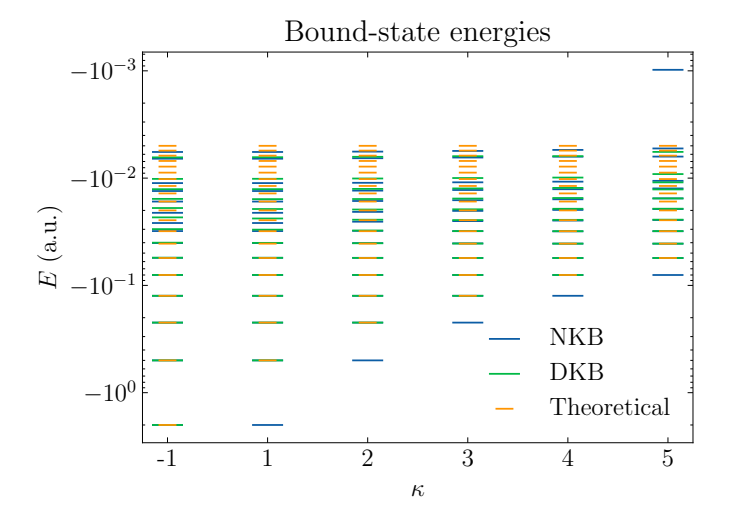
As we can see in figure 5a, for the largest basis sizes the error on the eigenvalues saturates, and becomes a decreasing function of the principal quantum number n. This can be explained by the fact that in the saturation region, the precision is limited by the imperfect representation of the singular behaviour of the wavefunction at $r \to 0$. Indeed, the ground state, having the highest probability density near the nucleus, is the most sensitive to this source of error and would require the finest knot distribution in this region.

In the figure 5b, we can see the variation of the error on n for different values of x_0 . The collapse of precision for n>20 is due to the characteristic size of the wavefunction increasing like n^2 , so that the chosen value of R_{max} becomes insufficient for highly excited states. The figure shows that the knot distribution can be adapted to be optimal for a specific value of n but cannot be optimal for all values of n. As stated before, our objective is to be able to represent the whole spectrum with good precision. For the range of states considered here, a value of x_0 around 10^{-5} would represent a good compromise.

Both the NKB and DKB methods can produce very good results, as we can see in figure 6a. The NKB method is observed to converge faster than the DKB method for the chosen parameter values, which remains to be explained, since DKB generally performs better. It is also less costly in terms of computational resources. The main drawback of the NKB



(a) Comparison of the convergence of the NKB and DKB methods for $s_{1/2}$ ($\kappa=-1$) bound-state energies. For $x_0=10^{-5}$ a.u. and $x_{max}=10^3$ a.u.



(b) Eigenvalues obtained from both methods compared to the theoretical values for a few values of the quantum number κ . A few eigenvalues obtained with the NKB method (appearing in blue) are not predicted by theory and correspond to spurious states. One example is the lowest $\kappa=1$ eigenvalue, which would correspond to a " $1p_{1/2}$ " state. For $x_0=1e-6$ and $x_{max}=200$ a.u.

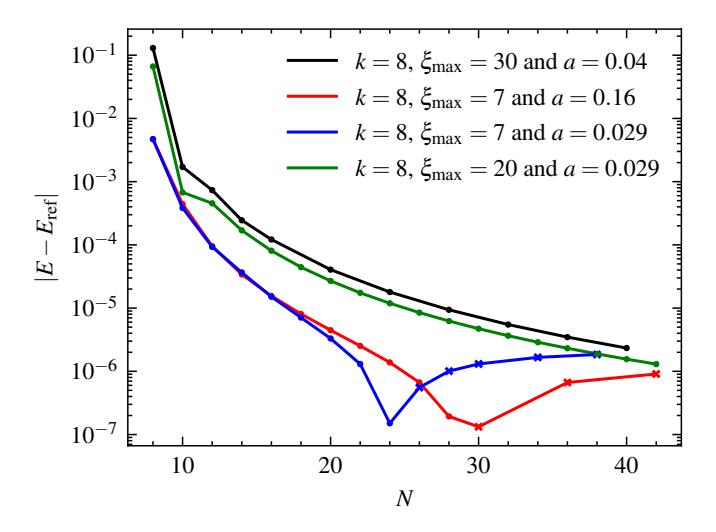
Figure 6: Comparison of the NKB and DKB methods.

method is that it produces spurious eigenvalues, which are not present in the DKB method [11]. The figure 6b shows the eigenvalues obtained with both methods for specific values of n and κ . For $\kappa=-1$, both methods produce very similar results, as seen in more detail in the figure 6a. However, for $\kappa\geq 1$, there is at least one spurious eigenvalue obtained with the NKB method. The DKB method does not produce any spurious eigenvalues, which is a significant advantage.

3.2 Results for H₂⁺

For this system, in the absence of analytical solutions, we have to rely on the literature to compare our results. We will use the results obtained by Nogueira [25].

At this point, only the NKB method has been implemented for the ${\rm H_2^+}$ system and only preliminary results have been obtained. Just like in the previous section, we need to optimize the different parameters to improve the accuracy of our results. This includes refining the distribution of knots, adjusting the grid size, and increasing the order of the B-spline functions. In a second phase, we will study the convergence of the method. The optimization of the parameters is done by studying only the error on the ground-state energy. As a consequence, the parameters won't be optimized for the entire spectrum, but this is a good first step to study the performance of our method. We will use mostly B-splines of order k=8 as it seems to be the best compromise between accuracy and computational resources. From a study of the error on the ground-state energy, we have found that the best parameters are: a=0.16 and $\xi_{\rm max}=7$. However, these parameters are not perfectly optimal as both have been determined independently using a low number of B-splines. It is possible that better parameters can be found by a global optimization for different numbers of basis functions. Still, we will use these parameters to run the convergence study .



Data 10^4 Fit: $\propto N^6$ 10^1 10^1 10 20 N

(a) Evolution of the difference of the ground-state energy from the literature value [25] for four sets of parameters, as a function of the number of B-splines (N) used for each radial variable (an equal number of B-splines is used for ξ and η). Dots correspond to a negative difference whereas crosses correspond to a positive difference. With $E_{\rm ref} = -1.102\ 641\ 581\ 032\ 577\ 164\ 12$ a.u. is the value from Ref. [25].

(b) Runtime as a function of N using the following sets of parameters: $k=8,\ \xi_{\rm max}=20$ and a=0.029 (green curve in fig. 7a).

Figure 7: Study of the convergence for the H_2^+ system for the lowest $j_z = 1/2$ eigenvalue with an internuclear distance R = 2.0.

The figure 7a shows the convergence of the ground-state energy for different sets of parameters. A minimal error of 1.5×10^{-7} a.u. is reached. However, when the number of B-splines is increased, for all the parameter sets the computed eigenvalue seems to converge towards a value that differs from the one reported in the literature by about 10^{-6} a.u. This is probably due to an error in the calculation of one (or several) matrix elements that have not been found yet. More computations could be done to characterize the problem more precisely, but the runtime scales like $\mathcal{O}(N^6)$, where N is the number of B-splines for each radial variable, resulting in long runtimes for large bases (see figure 7b). This problem should be investigated further before proceeding to the next step, which is the implementation of the DKB method for the H_2^+ system.

Conclusion

In this report, the current state of my work on the numerical resolution of the Dirac equation using B-spline functions has been presented. The focus was on the development and testing of two methods: the *No Kinetic Balance* (NKB) method and the *Dual Kinetic Balance* (DKB) method applied to two cases: the hydrogen atom and the hydrogen molecular ion H_2^+ . The goal is to obtain a precise numerical representation of the whole spectrum, which is crucial for the project's next step: the calculation of the one-loop self-energy correction.

The first step was to solve the Dirac equation for the hydrogen atom. This was done to validate the numerical methods and to evaluate their accuracy. The results obtained with both methods were compared to the analytical solution. Both methods yield very good results, with the DKB method having the important advantage that it does not produce spurious eigenvalues. The NKB method, however, is observed to converge faster and requires less computational resources. Both methods reach precisions that exceed the best results of numerical calculations reported in the literature, which is a significant achievement.

In a second step, we studied the ${\rm H}_2^+$ molecular ion, which is our main object of study. This is a more complex system, as the calculation of matrix elements involves multi-dimensional integrals, and the Dirac equation doesn't have an analytical solution. Only the NKB method has been implemented for now. The initial results are encouraging. However, they seem to indicate an error in the code, causing the results to converge to a wrong value. Currently, the best precision achieved is around 1.5×10^{-7} a.u. for the ground-state energy, which is not sufficient for the intended purpose. Moreover, the resolution has been done only for $j_z=1/2$ states. Further work is needed to extend the method to other values of j_z and to optimize the knot distribution for these different cases.

The long-term goal of this project is the numerical calculation of the one-loop self-energy correction. The objective is to achieve theoretical predictions of the energy levels that match or exceed the current experimental results for the hydrogen molecular ion H_2^+ and its isotopologues.

I will have the opportunity to continue this work for the next three years as a PhD student in the *LKB* group. This will allow me to further develop the numerical methods and to explore new avenues for improving the precision of the theoretical calculations. My ultimate goal is to contribute to the understanding of fundamental physics and to improve the value's precision of m_e/m_p .

References

- [1] P. J. Mohr, D. B. Newell, B. N. Taylor, and E. Tiesinga, "CODATA recommended values of the fundamental physical constants: 2022", Reviews of Modern Physics, Apr. 30, 2025. DOI: 10.1103/RevModPhys.97.025002. [Online]. Available: https://link.aps.org/doi/10.1103/RevModPhys.97.025002.
- [2] V. I. Korobov and J.-P. Karr, "Ro-vibrational spin-averaged transitions in the hydrogen molecular ions", Physical Review A, Sep. 7, 2021, ISSN: 2469-9926, 2469-9934. DOI: 10.1103/PhysRevA.104.032806. arXiv: 2107.14497 [physics]. [Online]. Available: http://arxiv.org/abs/2107.14497.
- [3] V. Q. Tran, J.-P. Karr, A. Douillet, J. C. J. Koelemeij, and L. Hilico, "Two-photon spectroscopy of trapped HD+ ions in the Lamb-Dicke regime", *Physical Review A*, Sep. 24, 2013. DOI: 10.1103/PhysRevA.88.033421. [Online]. Available: https://link.aps.org/doi/10.1103/PhysRevA.88.033421.
- [4] S. Alighanbari, M. G. Hansen, V. I. Korobov, and S. Schiller, "Rotational spectroscopy of cold and trapped molecular ions in the Lamb-Dicke regime", *Nature Physics*, Jun. 2018, ISSN: 1745-2481. DOI: 10.1038/s41567-018-0074-3. [Online]. Available: https://www.nature.com/articles/s41567-018-0074-3.
- [5] S. Alighanbari, I. V. Kortunov, G. S. Giri, and S. Schiller, "Test of charged baryon interaction with high-resolution vibrational spectroscopy of molecular hydrogen ions", *Nature Physics*, Sep. 2023, ISSN: 1745-2481. DOI: 10.1038/s41567-023-02088-2. [Online]. Available: https://www.nature.com/articles/s41567-023-02088-2.
- [6] S. Patra, M. Germann, J.-P. Karr, et al., "Protonelectron mass ratio from laser spectroscopy of HD+ at the part-per-trillion level", Science, Sep. 4, 2020. DOI: 10.1126/science.aba0453. [Online]. Available: https://www.science.org/doi/10.1126/ science.aba0453.
- [7] U. D. Jentschura, P. J. Mohr, and G. Soff, "Calculation of the Electron Self-Energy for Low Nuclear Charge", *Physical Review Letters*, Jan. 4, 1999. DOI: 10.1103/PhysRevLett.82.53. [Online]. Avail-

- able: https://link.aps.org/doi/10.1103/PhysRevLett.82.53.
- [8] W. Greiner, Relativistic Quantum Mechanics. Wave Equations / SpringerLink. [Online]. Available: https: //link.springer.com/book/10.1007/978-3-662-04275-5.
- [9] I. P. Grant and H. M. Quiney, "Rayleigh-Ritz approximation of the Dirac operator in atomic and molecular physics", *Physical Review A*, Jul. 2000, Publisher: American Physical Society. DOI: 10.1103/PhysRevA. 62.022508. [Online]. Available: https://link.aps.org/doi/10.1103/PhysRevA.62.022508.
- [10] Q. Sun, W. Liu, and W. Kutzelnigg, "Comparison of restricted, unrestricted, inverse, and dual kinetic balances for four-component relativistic calculations", *Theoretical Chemistry Accounts*, Jun. 2011, ISSN: 1432-2234. DOI: 10.1007/s00214-010-0876-6.
 [Online]. Available: https://doi.org/10.1007/s00214-010-0876-6.
- [11] V. M. Shabaev, I. I. Tupitsyn, V. A. Yerokhin, G. Plunien, and G. Soff, "Dual Kinetic Balance Approach to Basis-Set Expansions for the Dirac Equation", *Physical Review Letters*, Sep. 2004, Publisher: American Physical Society. DOI: 10.1103/PhysRevLett.93.130405. [Online]. Available: https://link.aps.org/doi/10.1103/PhysRevLett.93.130405.
- [12] P. J. Mohr, "Self-energy radiative corrections in hydrogen-like systems", Annals of Physics, Nov. 1974, ISSN: 0003-4916. DOI: 10.1016/0003-4916(74) 90398-4. [Online]. Available: https://www.sciencedirect.com/science/article/pii/ 0003491674903984.
- I. P. Grant, Ed., Relativistic Quantum Theory of Atoms and Molecules (Springer Series on Atomic, Optical, and Plasma Physics). Springer, 2007, ISBN: 978-0-387-34671-7. DOI: 10.1007/978-0-387-35069-1.
 [Online]. Available: http://link.springer.com/10.1007/978-0-387-35069-1.
- 14] C. d. Boor, A practical guide to splines, Revised ed. édition. Springer-Verlag New York Inc., Aug. 1994, ISBN: 978-0-387-90356-9. [Online]. Available: https://link.springer.com/book/9780387953663.

- [15] H. Bachau, E. Cormier, P. Decleva, J. E. Hansen, and F. Martín, "Applications of B-splines in atomic and molecular physics", Reports on Progress in Physics, Nov. 2001, ISSN: 0034-4885. DOI: 10.1088/0034-4885/64/12/205. [Online]. Available: https://dx. doi.org/10.1088/0034-4885/64/12/205.
- [16] M. Aubert-Frécon and C. Le Sech, "Correlated prolate-spheroidal wave function for two-electron diatomic systems", The Journal of Chemical Physics, Mar. 1981, ISSN: 0021-9606. DOI: 10.1063/1.441414.
 [Online]. Available: https://doi.org/10.1063/1.441414.
- [17] L. Yang, D. Heinemann, and D. Kolb, "Fully numerical relativistic calculations for diatomic molecules using the finite-element method", *Physical Review A*, Oct. 1993, Publisher: American Physical Society. DOI: 10.1103/PhysRevA.48.2700. [Online]. Available: https://link.aps.org/doi/10.1103/PhysRevA.48.2700.
- [18] W. R. Inc., Mathematica, Version 14.2, Champaign, IL, 2024. [Online]. Available: https://www.wolfram. com/mathematica.
- [19] D. H. Bailey, Mpfun2020: A thread-safe arbitrary precision package with special functions, All-Fortran and MPFR-based versions, full documentation available, Lawrence Berkeley National Laboratory, May 2024. [Online]. Available: https://www.davidhbailey.com/dhbpapers/mpfun2020.pdf.
- [20] E. Anderson, Z. Bai, C. Bischof, et al., LAPACK Users' Guide, Third. Society for Industrial and Applied Mathematics, 1999, ISBN: 0-89871-447-8 (paper-

- back). [Online]. Available: https://www.netlib.org/lapack/lug/.
- [21] B. Thaller, The Dirac Equation. Springer, 1992, ISBN: 978-3-642-08134-7 978-3-662-02753-0. DOI: 10.1007/978-3-662-02753-0. [Online]. Available: http://link.springer.com/10.1007/978-3-662-02753-0.
- [22] A. Messiah, Mécanique quantique Tome II, [Edition corrigée et améliorée]. Dunod, 1964, ISBN: 978-2100046959.
- [23] W. R. Johnson, S. A. Blundell, and J. Sapirstein, "Finite basis sets for the Dirac equation constructed from B splines", *Physical Review A*, Jan. 1988, Publisher: American Physical Society. DOI: 10.1103/PhysRevA. 37.307. [Online]. Available: https://link.aps.org/doi/10.1103/PhysRevA.37.307.
- [24] C. F. Fischer and F. A. Parpia, "Accurate spline solutions of the radial Dirac equation", Physics Letters A, Aug. 1993, ISSN: 0375-9601. DOI: 10.1016/0375-9601(93) 91138-U. [Online]. Available: https://www.sciencedirect.com/science/article/pii/037596019391138U.
- [25] H. Demattos Nogueira, "Dirac equation in hydrogen molecular ions for the calculation of QED corrections", These de doctorat, Sorbonne université, Feb. 27, 2024. [Online]. Available: https://theses.fr/2024SORUS050.
- [26] M. Salman, "Quantum Electrodynamic Corrections in Quantum Chemistry", Ph.D. dissertation, Université Paul Sabatier - Toulouse III, Jan. 28, 2022. [Online]. Available: https://theses.hal.science/tel-03715663.

Appendix

A Matrix Elements of the Dirac Equation for the Hydrogen Atom in DKB

In this section, we present the matrix elements of the Dirac equation for the hydrogen atom in the DKB (Dual Kinetic Balance) method.

The DKB conditions are expressed by relationships between basis functions representing the large and small components of the wave function. The two-component radial wavefunction is expanded as follows:

$$\phi = \sum_{i=1}^{N} a_i^+ \begin{bmatrix} \pi_i^+ \\ \frac{\boldsymbol{\sigma} \cdot \boldsymbol{p}}{2mc} \ \pi_i^+ + \sum_{i=1}^{N} a_i^- \begin{bmatrix} -\frac{\boldsymbol{\sigma} \cdot \boldsymbol{p}}{2mc} \ \pi_i^- \end{bmatrix} \end{bmatrix}$$

Applying these conditions, one obtains the following eigenvalue problem (note the slightly different notations with respect to 2.16; here we use the notations from Maen Salman's thesis [26]).

$$H\mathbf{c} = ES\mathbf{c}$$

where H is the $(2N \times 2N)$ Hamiltonian matrix, E is the energy, S is the overlap matrix, and c is a column vector containing the expansion coefficients a_i^+ , a_i^- .

The different elements are defined as follows:

$$H = \begin{bmatrix} mc^{2}S^{+} + \frac{3}{2}T^{+} - eV^{+} - \frac{e\hbar^{2}}{4m^{2}c^{2}}W^{+} & \frac{\hbar}{2mc}\left[-eA^{+} + B^{+}\right] \\ \frac{\hbar}{2mc}\left[-eA^{-} - B^{-}\right] & -mc^{2}S^{-} - \frac{3}{2}T^{-} - eV^{-} - \frac{e\hbar^{2}}{4m^{2}c^{2}}W^{-} \end{bmatrix}$$

$$S = \begin{bmatrix} S^{+} + \frac{1}{2mc^{2}}T^{+} & 0 \\ 0 & S^{-} + \frac{1}{2mc^{2}}T^{-} \end{bmatrix}$$

with:

$$\begin{split} [S^\pm]_{i,j} &= \int_0^\infty \pi_i^\pm \pi_j^\pm dr \\ [V^\pm]_{i,j} &= \int_0^\infty \pi_i^\pm V\left(r\right) \pi_j^\pm dr \\ [T^\pm]_{i,j} &= \frac{-\hbar^2}{2m} \int_0^\infty \pi_i^\pm \left[\frac{d^2}{dr^2} \pi_j^\pm \mp \frac{\kappa \left(1 \pm \kappa\right)}{r^2} \pi_j^\pm\right] dr \\ [W^\pm]_{i,j} &= \int_0^\infty \left[\frac{d}{dr} \pi_i^\pm \pm \frac{\kappa}{r} \pi_i^\pm\right] V\left(r\right) \left[\frac{d}{dr} \pi_j^\pm \pm \frac{\kappa}{r} \pi_j^\pm\right] dr \\ [A^\pm]_{i,j} &= \int_0^\infty \pi_i^\pm V\left(r\right) \left[\frac{d}{dr} \pi_j^\mp \mp \frac{\kappa}{r} \pi_j^\mp\right] dr + \int_0^\infty \left[\frac{d}{dr} \pi_i^\pm \pm \frac{\kappa}{r} \pi_i^\pm\right] V\left(r\right) \pi_j^\mp dr \\ [B^\pm]_{i,j} &= \frac{\hbar^2}{2m} \int_0^\infty \left[\frac{d}{dr} \pi_i^\pm \pm \frac{\kappa}{r} \pi_i^\pm\right] \left[\frac{d^2}{dr^2} \pi_j^\mp \pm \frac{\kappa \left(1 \mp \kappa\right)}{r^2} \pi_j^\mp\right] dr \end{split}$$

B B-Splines: Illustrative Examples

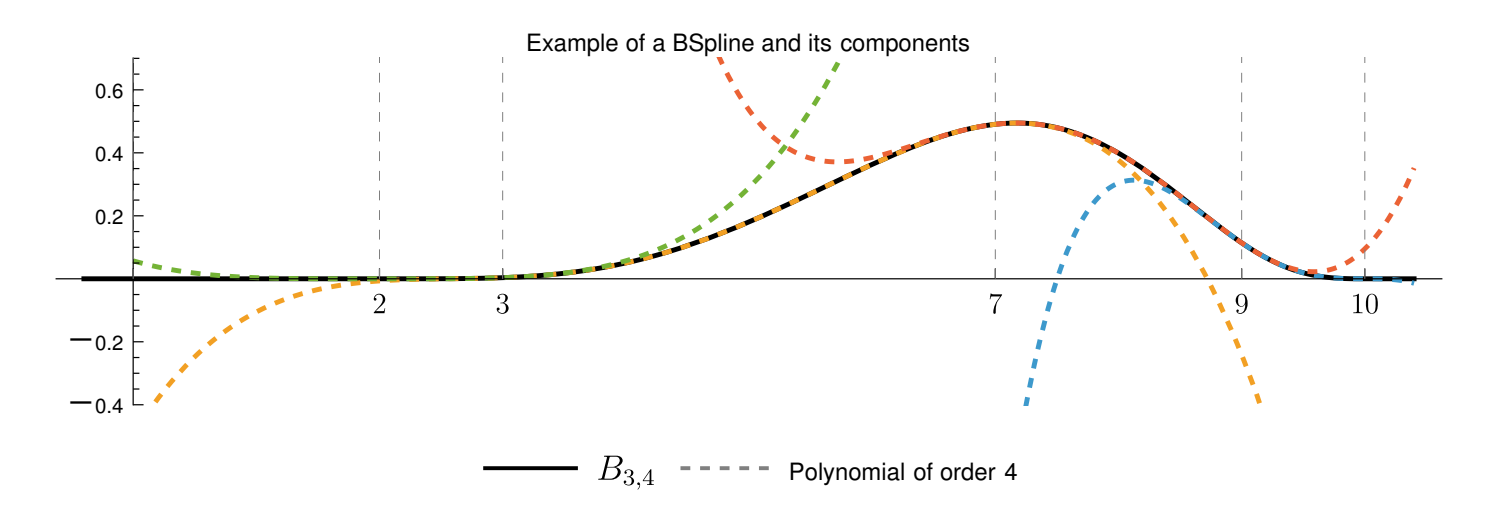


Figure B-1: Presentation of B-Spline Function for a random set of knots and its different polynomials.

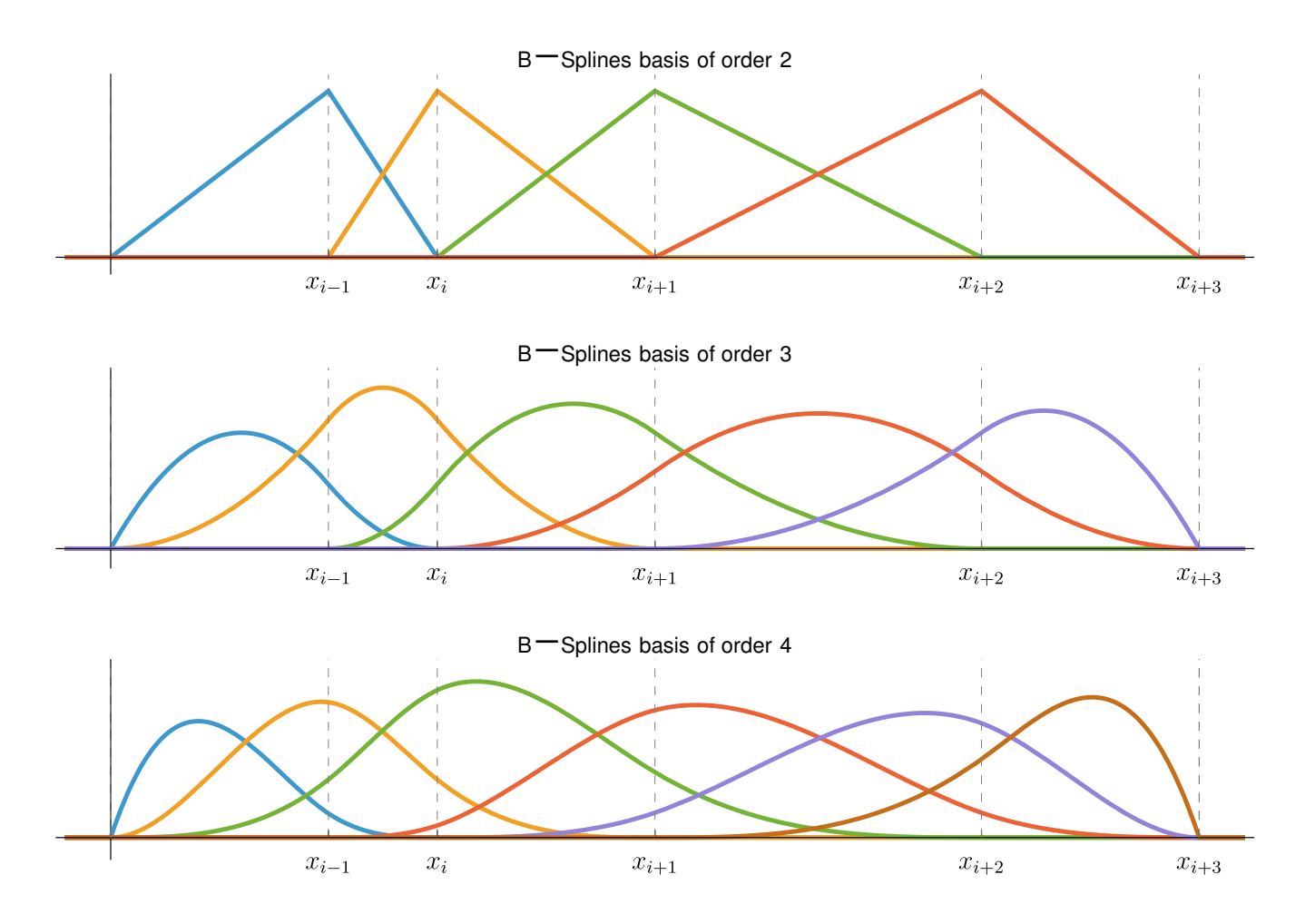


Figure B-2: Presentation of three complete B-Spline bases for k = 2, 3, 4 with a random set of knots.

C Prolate Spheroidal Coordinates

A 3D-coordinate system $(\eta, \xi \text{ and } \theta)$ with one parameter R:

$$\xi = \frac{1}{2R} \left(\sqrt{x^2 + y^2 + (z+R)^2} + \sqrt{x^2 + y^2 + (z-R)^2} \right)$$

$$\eta = \frac{1}{2R} \left(\sqrt{x^2 + y^2 + (z+R)^2} - \sqrt{x^2 + y^2 + (z-R)^2} \right)$$

$$\theta = \arctan \frac{y}{x}$$

with $\xi \in [1, \infty)$, $\eta \in [-1, 1]$ and $\theta \in [0, 2\pi[$.

Reciprocally, we have:

$$x = R\sqrt{(\xi^2 - 1)(1 - \eta^2)}\cos\theta$$
$$y = R\sqrt{(\xi^2 - 1)(1 - \eta^2)}\sin\theta$$
$$z = R\xi\eta$$

C.1 Partial Derivatives

Relationship To Cartesian Coordinates:

$$\begin{split} \frac{\partial}{\partial x} &= \frac{\cos \theta}{R(\xi^2 - \eta^2)} \left[\sqrt{1 - \eta^2} \xi \frac{\partial}{\partial \xi} + \sqrt{\xi^2 - 1} \eta \frac{\partial}{\partial \eta} \right] - \frac{\sin \theta}{R\sqrt{(\xi^2 - 1)(1 - \eta^2)}} \frac{\partial}{\partial \theta} \\ \frac{\partial}{\partial y} &= \frac{\sin \theta}{R(\xi^2 - \eta^2)} \left[\sqrt{1 - \eta^2} \xi \frac{\partial}{\partial \xi} + \sqrt{\xi^2 - 1} \eta \frac{\partial}{\partial \eta} \right] + \frac{\cos \theta}{R\sqrt{(\xi^2 - 1)(1 - \eta^2)}} \frac{\partial}{\partial \theta} \\ \frac{\partial}{\partial z} &= \frac{1}{R(\xi^2 - \eta^2)} \left[\eta \sqrt{\xi^2 - 1} \frac{\partial}{\partial \xi} + \xi \sqrt{1 - \eta^2} \frac{\partial}{\partial \eta} \right] \end{split}$$

Relationship To Cylindrical Coordinates:

$$\partial_r = \frac{\sqrt{(\xi^2 - 1)(1 - \eta^2)}}{R(\xi^2 - \eta^2)} \left[\xi \partial_{\xi} - \eta \partial_{\eta} \right]$$

C.2 Jacobian, Vector Fields and Differential Operators

Jacobian and Inverse Jacobian Matrices:

$$\begin{pmatrix} \hat{\boldsymbol{x}} \\ \hat{\boldsymbol{y}} \\ \hat{\boldsymbol{z}} \end{pmatrix} = \begin{pmatrix} \sqrt{1 - \eta^2} \xi R \cos(\theta) & \eta \sqrt{\xi^2 - 1} R \cos(\theta) & -\sqrt{1 - \eta^2} \sqrt{\xi^2 - 1} R \sin(\theta) \\ \sqrt{1 - \eta^2} \xi R \sin(\theta) & \eta \sqrt{\xi^2 - 1} R \sin(\theta) & \sqrt{1 - \eta^2} \sqrt{\xi^2 - 1} R \cos(\theta) \\ -\eta \sqrt{\xi^2 - 1} R & \sqrt{1 - \eta^2} \xi R & 0 \end{pmatrix} \begin{pmatrix} \hat{\boldsymbol{\xi}} \\ \hat{\boldsymbol{\eta}} \\ \hat{\boldsymbol{\theta}} \end{pmatrix}$$

$$\begin{pmatrix} \hat{\boldsymbol{\xi}} \\ \hat{\boldsymbol{\eta}} \\ \hat{\boldsymbol{\theta}} \end{pmatrix} = \begin{pmatrix} \frac{\sqrt{1-\eta^2 \xi \cos(\theta)}}{R(\xi^2-\eta^2)} & \frac{\sqrt{1-\eta^2 \xi \sin(\theta)}}{R(\xi^2-\eta^2)} & \frac{\eta\sqrt{\xi^2-1}}{R(\xi^2-\eta^2)} \\ \frac{\eta\sqrt{\xi^2-1}\cos(\theta)}{R(\xi^2-\eta^2)} & \frac{\eta\sqrt{\xi^2-1}\sin(\theta)}{R(\xi^2-\eta^2)} & -\frac{\sqrt{1-\eta^2 \xi}}{R(\xi^2-\eta^2)} \\ -\frac{\sin(\theta)}{R\sqrt{(\xi^2-1)(1-\eta^2)}} & \frac{\cos(\theta)}{R\sqrt{(\xi^2-1)(1-\eta^2)}} & 0 \end{pmatrix} \begin{pmatrix} \hat{\boldsymbol{x}} \\ \hat{\boldsymbol{y}} \\ \hat{\boldsymbol{z}} \end{pmatrix}$$

Vector Field Relation:

$$\vec{A} = A_{\xi}\hat{\xi} + A_{\eta}\hat{\eta} + A_{\theta}\hat{\theta}$$

$$\Rightarrow \begin{cases} A_{\xi} = \left[R\xi\sqrt{1-\eta^2} \left(A_x \cos\theta + A_y \sin\theta \right) - RA_z \eta \left(\xi^2 - 1 \right) \right] \\ A_{\eta} = \left[R\eta\sqrt{\xi^2 - 1} \left(A_x \cos\theta + A_y \sin\theta \right) - RA_z \xi \left(1 - \eta^2 \right) \right] \\ A_{\theta} = R\sqrt{\left(\xi^2 - 1 \right) \left(1 - \eta^2 \right)} \left(A_y \cos\theta - A_x \sin\theta \right) \end{cases}$$

$$\Rightarrow \begin{cases} A_x = \frac{\cos(\theta)}{R(\xi^2 - \eta^2)} \left(\sqrt{1 - \eta^2} \xi A_{\xi} + \eta \sqrt{\xi^2 - 1} A_{\eta} \right) - \frac{\sin(\theta)}{R\sqrt{(\xi^2 - 1)(1 - \eta^2)}} A_{\theta} \\ A_y = \frac{\sin(\theta)}{R(\xi^2 - \eta^2)} \left(\sqrt{1 - \eta^2} \xi A_{\xi} + \eta \sqrt{\xi^2 - 1} A_{\eta} \right) + \frac{\cos(\theta)}{R\sqrt{(\xi^2 - 1)(1 - \eta^2)}} A_{\theta} \\ A_z = \frac{1}{R(\xi^2 - \eta^2)} \left(\eta \sqrt{\xi^2 - 1} A_{\xi} - \sqrt{1 - \eta^2} \xi A_{\eta} \right) \end{cases}$$

Gradient:

$$\nabla f = \frac{\xi^2 \left(1 - \eta^2\right) - \eta^2 \left(\xi^2 - 1\right)}{\xi^2 - \eta^2} \partial_{\xi} f \hat{\boldsymbol{\xi}} + \frac{\xi^2 \left(1 - \eta^2\right) + \eta^2 \left(\xi^2 - 1\right)}{\xi^2 - \eta^2} \partial_{\eta} f \hat{\boldsymbol{\eta}} + \partial_{\theta} f \hat{\boldsymbol{\theta}}$$

Laplace Operator:

$$\begin{split} \nabla^2 \Phi = & \frac{1}{R^2 (\xi^2 - \eta^2)} \left\{ \frac{\partial}{\partial \xi} \left[\left(\xi^2 - 1 \right) \frac{\partial \Phi}{\partial \xi} \right] + \frac{\partial}{\partial \eta} \left[(1 - \eta^2) \frac{\partial \Phi}{\partial \eta} \right] \right\} \\ & + \frac{1}{R^2 (\xi^2 - 1) (1 - \eta^2)} \frac{\partial^2 \Phi}{\partial \theta^2} \end{split}$$

D Example: Integration of element $C_{22}^{(3)}$

In this section, we will provide an example of how to integrate one of the matrix elements used in the numerical resolution of the Dirac equation using B-spline functions. We will solve the element $C_{22}^{(3)}$ of the matrix C for H_2^+ . From (2.21), we have:

$$\left[\mathbf{C}_{22}^{(3)}\right]_{ij} = -\int B_i^{(2)} \partial_z \left\{ B_j^{(2)} \right\} d^3 x$$

where i and j are the indices of the B-spline basis functions involved in the integration.

We can replace the volume element d^3x by its expression in spheroidal prolate coordinates, the B-spline basis functions by their expression in these coordinates and the partial derivative ∂_z by its expression in these coordinates. The integral then becomes:

$$\begin{split} \left[\mathbf{C}_{22}^{(3)} \right]_{ij} &= -2\pi R^3 \int B_i^{(2)} \partial_z \left\{ B_j^{(2)} \right\} \left(\xi^2 - \eta^2 \right) d\xi d\eta \\ &= -2\pi R^2 \int b_{i'}^{k_\eta} b_i^{k_\xi} \left(\left(\xi^2 - 1 \right) \left(1 - \eta^2 \right) \right)^{j_z + \frac{1}{2}} \\ &\cdot \left(\left(j_z + \frac{1}{2} \right) \eta \xi \left(\underbrace{b_{j'}^{k_\eta} b_j^{k_\xi} - b_j^{k_\xi} b_{j'}^{k_\eta}} \right) + \eta (\xi^2 - 1) b_{j'}^{k_\eta} \partial_\xi b_j^{k_\xi} + \xi (1 - \eta^2) b_j^{k_\xi} \partial_\eta b_{j'}^{k_\eta} \right) d\xi d\eta \end{split}$$

Now, we need to fix the value of j_z to compute the integral. For example, if we take $j_z=\frac{1}{2}$, we have :

$$\begin{split} \left[\mathbf{C}_{22}^{(3)} \right]_{ij} &= -2\pi R^3 \int B_i^{(2)} \partial_z \left\{ B_j^{(2)} \right\} \left(\xi^2 - \eta^2 \right) d\xi d\eta \\ &= -2\pi R^2 \int \sqrt{(\xi^2 - 1) \left(1 - \eta^2 \right)} b_i^\xi b_i^\eta \left(\left(\xi^2 - 1 \right) \eta \sqrt{(1 - \eta^2)} b_j^\eta \partial_\xi \left(\sqrt{(\xi^2 - 1)} b_j^\xi \right) \right. \\ &+ \left. \left(1 - \eta^2 \right) \xi \sqrt{(\xi^2 - 1)} b_j^\xi \partial_\eta \left(\sqrt{(1 - \eta^2)} b_j^\eta \right) \right) d\xi d\eta \\ &= -2\pi R^2 \int \sqrt{(\xi^2 - 1) \left(1 - \eta^2 \right)} b_i^\xi b_i^\eta \left(\left(\xi^2 - 1 \right) \eta \sqrt{(\xi^2 - 1) \left(1 - \eta^2 \right)} b_j^\eta \left(\frac{\xi}{(\xi^2 - 1)} b_j^\xi + \partial_\xi b_j^\xi \right) \\ &+ \left(1 - \eta^2 \right) \xi \sqrt{(\xi^2 - 1) \left(1 - \eta^2 \right)} b_j^\xi \left(\partial_\eta b_j^\eta - \frac{\eta}{(1 - \eta^2)} b_j^\eta \right) \right) d\xi d\eta \\ &= -2\pi R^2 \int \left(\xi^2 - 1 \right) \left(1 - \eta^2 \right) b_i^\xi b_i^\eta \left(\eta b_j^\eta \xi b_j^\xi + \eta b_j^\eta \left(\xi^2 - 1 \right) \partial_\xi b_j^\xi + \xi b_j^\xi \left(1 - \eta^2 \right) \partial_\eta b_j^\eta - \xi b_j^\xi \eta b_j^\eta \right) d\xi d\eta \end{split}$$

At this point, we can see that the integral is separable in ξ and η , which allows us to compute it more easily. Thus, we can write:

$$\begin{split} \left[\mathbf{C}_{22}^{(3)}\right]_{ij} &= -2\pi R^2 \int \left(\xi^2 - 1\right)^2 b_i^{\xi} \partial_{\xi} b_j^{\xi} \left(1 - \eta^2\right) \eta b_i^{\eta} b_j^{\eta} d\xi d\eta + \int \left(\xi^2 - 1\right) \xi b_i^{\xi} b_j^{\xi} \left(1 - \eta^2\right)^2 b_i^{\eta} \partial_{\eta} b_j^{\eta} d\xi d\eta \\ &= \boxed{-2\pi R^2 \int \left(\xi^2 - 1\right)^2 b_i^{\xi} \partial_{\xi} b_j^{\xi} d\xi \int \left(1 - \eta^2\right) \eta b_i^{\eta} b_j^{\eta} d\eta + \int \left(\xi^2 - 1\right) \xi b_i^{\xi} b_j^{\xi} d\xi \int \left(1 - \eta^2\right)^2 b_i^{\eta} \partial_{\eta} b_j^{\eta} d\eta} \end{split}$$

Now, we focus on one specific element of the mesh, denoting by a_{α} , b_{β} , c_{χ} , and d_{δ} the coefficients of the four involved B-spline functions:

$$\left[\mathbf{C}_{22}^{(3)}\right]_{ij} = -2\pi R^2 \int \left(\xi^2 - 1\right)^2 \left(\sum_{\alpha} a_{\alpha} \xi^{\alpha}\right) \partial_{\xi} \left(\sum_{\chi} c_{\chi} \xi^{\chi}\right) d\xi \int \left(1 - \eta^2\right) \eta \left(\sum_{\beta} b_{\beta} \eta^{\beta}\right) \left(\sum_{\delta} d_{\delta} \eta^{\delta}\right) d\eta$$

$$\begin{split} &+\int \left(\xi^2-1\right)\xi\left(\sum_{\alpha}a_{\alpha}\xi^{\alpha}\right)\left(\sum_{\chi}c_{\chi}\xi^{\chi}\right)d\xi\int\left(1-\eta^2\right)^2\left(\sum_{\beta}b_{\beta}\eta^{\beta}\right)\partial_{\eta}\left(\sum_{\delta}d_{\delta}\eta^{\delta}\right)d\eta\\ &=-2\pi R^2\sum_{\alpha,\beta,\chi,\delta}a_{\alpha}b_{\beta}c_{\chi}d_{\delta}\left[\int\left(\xi^2-1\right)^2\xi^{\alpha}\partial_{\xi}\xi^{\chi}d\xi\int\left(1-\eta^2\right)\eta^{1+\beta+\delta}d\eta\\ &+\int\left(\xi^2-1\right)\xi^{1+\alpha+\chi}d\xi\int\left(1-\eta^2\right)^2\eta^{\beta}\partial_{\eta}\eta^{\delta}d\eta\right]\\ &=-2\pi R^2\sum_{\alpha,\beta,\chi,\delta}a_{\alpha}b_{\beta}c_{\chi}d_{\delta}\left[\chi\int\left(\xi^2-1\right)^2\xi^{\alpha+\chi-1}d\xi\int\left(1-\eta^2\right)\eta^{1+\beta+\delta}d\eta\\ &+\delta\int\left(\xi^2-1\right)\xi^{1+\alpha+\chi}d\xi\int\left(1-\eta^2\right)^2\eta^{\beta+\delta-1}d\eta\right]\\ &=-2\pi R^2\sum_{\alpha,\beta,\chi,\delta}a_{\alpha}b_{\beta}c_{\chi}d_{\delta}\cdot\xi^{\alpha+\chi}\eta^{\beta+\delta}\left[\chi\left(\frac{1}{\alpha+\chi}-\frac{2\xi^2}{2+\alpha+\chi}+\frac{\xi^4}{4+\alpha+\chi}\right)\left(\frac{\eta^4}{4+\beta+\delta}-\frac{\eta^2}{2+\beta+\delta}\right)\\ &+\delta\left(\frac{\xi^4}{\alpha+\chi+4}-\frac{\xi^2}{\alpha+\chi+2}\right)\left(\frac{\eta^4}{\beta+\delta+4}-\frac{2\eta^2}{\beta+\delta+2}+\frac{1}{\beta+\delta}\right)\right] \end{split}$$

This last expression gives us the value of the element $\mathbf{C}_{22}^{(3)}$ for the specific indices i and j. It can easily be evaluated numerically by substituting the coefficients a_{α} , b_{β} , c_{χ} , and d_{δ} with their respective values for the B-spline basis functions involved in the integration. This process can be repeated for all elements of the matrix \mathbf{C} , allowing us to construct the full matrix needed for the numerical resolution of the Dirac equation.

The expressions are also verified using the symbolic computation software Mathematica.